



UNIVERSITY OF CRETE
PHYSICS DEPARTMENT



Foundation for Research and Technology Hellas Institute of Electronic Structure & Laser

PHD THESIS BY PROTOPAPPA NEKTARIA

Femtosecond Laser Induced Periodic Surface Structures on Polymer surface

Supervisor: Dr. Emmanuel Stratakis

Heraklion, Crete 2022

Table of Contents

Thesis Summery.....	4
Introduction.....	5
Chapter 1: Basic principles of light-material interaction.....	6
1.1 Radiation by laser beam induce periodic surface structures (LIPPS).....	6
1.2 Physical mechanisms.....	7
1.2.1 Surface Plasmon Polaritons (SPP).....	8
1.2.2 Interference of surface plasmon with the laser beam.....	10
1.2.3 Two Temperature Model.....	10
1.2.3.1 TTM and femtosecond laser pulses.....	11
1.2.3.2 Combined TTM and Hydrodynamic effects.....	12
1.3.3 Dependence of periodicity on the number of the laser pulses.....	13
Chapter 2: Light polarization.....	14
Chapter 3: Experimental methods and analysis.....	16
3.1 Laser beam spatial profile.....	16
3.2 S-Waveplate polarization converter.....	17
3.3 Laser system - Experimental set up.....	18
3.4 Characterization methods.....	19
3.4.1 Period measurements & Fourier analysis.....	19
Two-dimensional fast Fourier transform surface image analysis.....	19
3.4.2 Characterization techniques.....	20
3.4.3 Pulse Calculation.....	21
3.4.4 Laser fluence calculation.....	22
Chapter 4: Parametrical study.....	24
4.1 LIPPS Formation on Polycarbonate using 3 rd harmonic and Analysis.....	24
4.2 LIPPS Formation on Polycarbonate using 4 th harmonic and Analysis.....	28
4.3 Dots Formation on Polycarbonate using 4 th harmonic and Analysis.....	32
Chapter 5: Structures' Properties.....	38
5.1 Ultraviolet-Visible spectroscopy analysis on ripples and dots.....	38

5.3 Fourier Transform Infrared measurements on ripples and dots.....	40
5.2 Contact angle measurements on ripples and dots.....	42
5.3 Cells' adhesion on ripples and dots.....	46
Conclusion.....	48
Bibliography.....	49
Acknowledgments.....	50

Thesis Summery

This thesis explores the formation of laser induced periodic surface structures (LIPPS) on Poly Carbonate (PC) bulk material by irradiation with femtosecond pulses of 342 and 257 nm and laser fluence above the ablation threshold. The morphological features of the structures can be affected by changes in polarization, laser wavelength, energy, etc. of the laser pulses, resulting in different surface structures.

In this study it is shown how changing the polarization from linear to circular can bring a new morphological outcome. Linear radiation results in periodic structures with one direction, while circular radiation shapes a different morphology of dot-like structures. Therefore, there were formed two different surfaces -LIPPS and Dots. To conclude to the suitable fluency areas and their limits, parametrical study was performed for both types of structures and the most uniform were tested for their hydrophobicity, their optical and cell adhesion properties.

Introduction

The ability to structure a morphologically new surfaces exclusively with laser light has gained significant attention due to the relative simplicity of the process itself and the remarkable functionalities that a material can attain by the changes in the surface morphological features. There are two ways to of laser surface modification: direct inscription and laser induced self-assembly.

Birnbaum observes periodically arranged structures, in the early sixties, following the irradiation of Germanium surfaces by pulsed ruby lasers and, since then, this kind of structures have been generated on a wide variety of materials under different conditions. These structures are commonly called “laser induced periodic surface structures”. A whole new field of research opened aiming to reproduce, explore the formation mechanism and reveal the properties that LIPPS can induce to a solid surface.

In recent years nanofabrication with femtosecond laser irradiation has raised much interest in surface nanostructures of metals, semiconductors, and polymers. Laser induced periodic surface structures (LIPPS) have been observed and reproduced by many authors. Despite the extensive studies on LIPPS, only few references report about LIPPS on polymers upon irradiation in the femtosecond regime. On the other hand, there is a wealth of information on polymers’ laser processing with UV-pulsed laser and pulse lengths of, typically, up to tens of nanoseconds at fluences both below and above the ablation threshold. Moreover, for polymers on the fs irradiation, LIPPS have mostly been detected at the bottom of ablation craters. Another way to form LIPPS on polymers is the scaffold method, where a laser processed metal where we have already produced LIPPS, is used as scaffold to “print” its pattern on polymers. However, we are talking about a time and money consuming method of non-direct laser process.

With this brief refence to the research of polymers on laser induced methods, it is clear the variety of additional research that can be done, on only for bibliographical reasons, but also practical. Their consequently large molecular mass, relative to small molecule compounds, produces unique physical properties including toughness, high elasticity, and viscoelasticity. All these properties combined with the surface properties that laser induced topography can provide, creates a sector of new applications and beneficial results.

The form and properties of each surface is affected by the periodicity of the morphology. In many materials such as metals, after exposure to linearly polarized radiation at normal incidence, the lateral period of the observed LIPPS is very close to the wavelength of the incident radiation. This type of structures is usually called low spatial frequency LIPPS (LSFL), and it will be discussed in this study. The interference model of LIPPS formation, represents a first-principle theory which takes into consideration the interaction of an electromagnetic wave with a microscopically rough surface plasmon polaritons (SPP). A theoretical attempt based on well-known models from hydrodynamics of thin films, consider the laser induced changes in the complex refractive index due to transient generation of quasi-free electrons in the conduction band of the solid. It has also been shown experimentally that the laser polarization plays a very important role to determine the orientation and final form of the ripples, so during this work we study two types of polarization: linear and circular and observe the differences in both their morphologies and properties.

Chapter 1: Basic principles of light-material interaction

1.1 Radiation by laser beam induce periodic surface structures (LIPPS)

The processing of solid surfaces using ultra-narrow laser pulses, causes a modification of the surface morphology with structural characteristics, making it functional for various applications. A type of structure are the surface periodic structures caused by the radiation (LIPPS) or otherwise wave-like structures (ripples). These structures display a uniform and periodical pattern with a relatively shallow depth, with a periodicity up to the wavelength of the laser beam.

Ripples are observed as high spatial frequency LIPPS (HSFL) or low spatial frequency LIPPS (LSFL). Both types exhibit a well-defined orientation with respect to a linear polarization state of the incident laser light and it has been also observed that they follow the electric fields orientation for other more complex polarization states. In the Figure 1.1 below we can see an example of those structures.

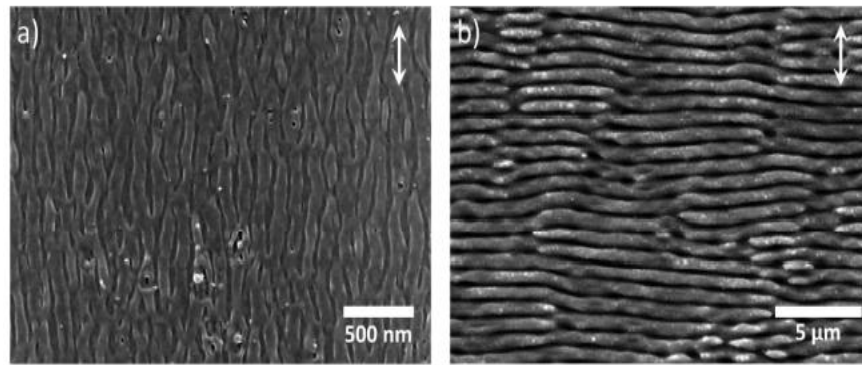


Figure 1.1: Top-view scanning electron microscopy images of two characteristic surface morphologies observed upon femtosecond laser scan processing of a Titanium surface (1026 nm, 170 fs, 1 kHz). (a) High spatial frequency LIPSS (HSFL), (b) Low spatial frequency LIPSS (LSFL). The double ended white arrow indicate the polarization state of the exciting laser source. In the right upper side of each image, we can see the direction of the incident's electric field

Characteristics such as the periodicity and the orientation of the ripples strongly depend on the irradiated material. For strongly absorbing materials (metals or semiconductors), near-wavelength sized LSFL are usually generated with an orientation perpendicular to the laser beam polarization. The periods are close to the laser wavelength and their specific value has been found to depend on the optical properties of the material, the pulse number, and the surface roughness. These structures are observed in the ablative regime for fluences up to several times the ablation threshold. For fluences very close to the ablation threshold, HSFL can be formed.

In the case of weakly absorbing materials (dielectrics), sub-wavelength sized LSFL are found mostly with an orientation parallel to the polarization. The periods are close to $\frac{\lambda}{n}$, with n being the refractive index of the material. The corresponding HSFL on dielectrics normally are oriented perpendicular to the polarization of the laser beam but sometimes also parallel. In this thesis we will focus on LSFL structures which were experimentally achieved and used for various properties measurements.

In Figure 1.2 we can see the interference patterns as a result of light interaction with randomly distributed holes and bumps below glass and metal surfaces. The radiative field patterns on metal surface are straight perpendicular to laser polarization, whereas the patterns on glass surface conserve more dominant

orientation parallel to laser polarization. As polymers properties are very much a like glass, we can consider the same behavior.

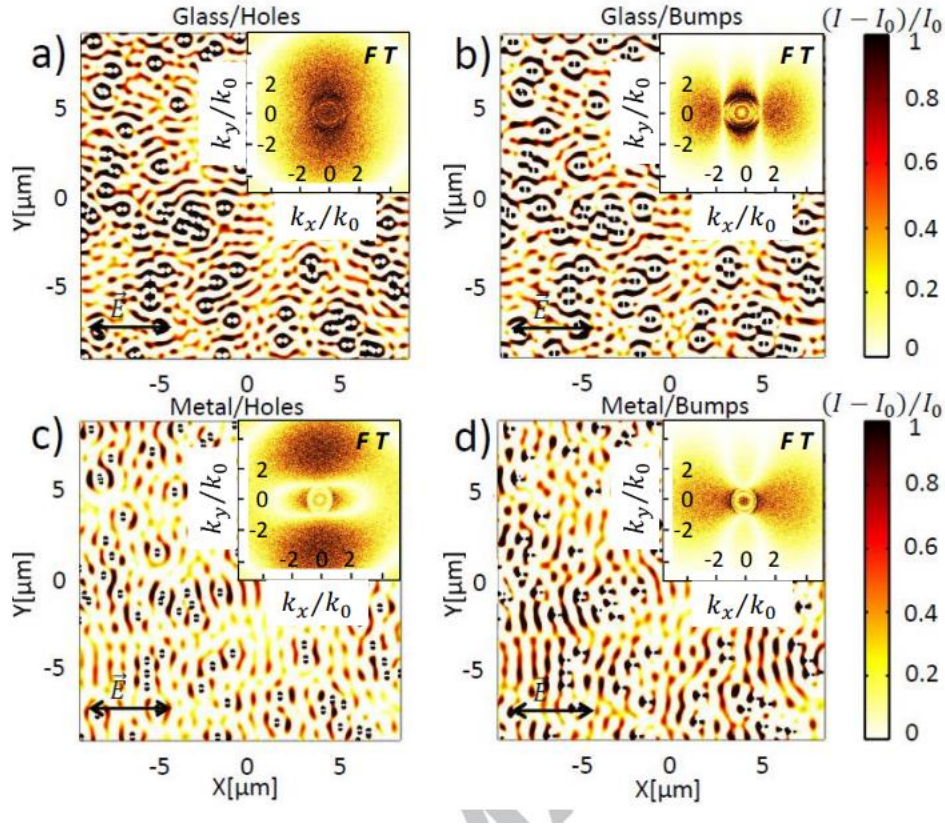


Figure 1.2 Absorbed energy distributions and their Fourier Transforms (FT) in the transverse plane on glass surface with (a) holes, (b) bumps and on metal surface with (c) holes, (d) bumps of $R = 20$ nm. $k_0 = 2\pi/\lambda$ is the wave-vector of propagation in air.

The average spacings on metal surface correspond to $\approx \lambda$, whereas the average spacings on glass surface are close to λ .

1.2 Physical mechanisms

According to this theoretical approach the creation of wavy structures attributes to the enhancing contribution of the incident beam with a surface-scattered electromagnetic wave. In this mechanism, the scattered electromagnetic wave caused by the surface roughness is the beam itself. More specifically, Emmony et al. in 1973 proposed the initial laser beam impinges on the rough surface causing its effect to appear diffusion and rays to be scattered in different directions. Then, an additional pulse contributes amplifying with a scattered beam, causing a maximization of the radiation intensity, which will lead to the creation of the structure. The period (Λ) of the wave structures in this mechanism is calculated from the relation:

$$\Lambda = \frac{\lambda}{1 \pm \sin\theta} \quad \text{Eq. 1}$$

with λ been the laser beam wavelength and θ the angle of the incident beam. For a vertical angle of incidence, the equation takes the form $\Lambda \approx \lambda$. So, this mechanism describes the low-frequency wave

structures, ideally when the deviations of the periods of the structures from the wavelength of the laser beam are very small.

Later, Sipe et al. reported an until today well-established formation mechanism of surface structures. They claimed that the energy deposition on a rough surface (depending on the wavelength) is not homogeneous and introduced an “efficacy factor”, η . Moreover, that strong peak of the electromagnetic field inducing the periodic surface patterns with specific orientation depends not only on the angle of the incidence but also on the polarization of the laser with the surface-scattered wave originates the LIPPS formation. It didn't take long for the surface-scattered wave scenario to be replaced with the proposition that the incident laser beam interferes with surface electron density waves commonly called as surface plasmon polariton waves (SPPs).

Another important contribution was from Huang et. Al who reported a multiple pulse feedback mechanism in which they considered that the ripples result from the initial direct SPPs-laser interference and the subsequent grating-assisted SPP-laser coupling.

The origin of LIPPS is still debatable, since there is not yet reported a single theoretical model that can account and predict all classes of LIPPS. One other process is also required in order to cause dramatic change in the surface morphological profile (i.e., melting) that will eventually lead to a surface modification that will change the relief.

1.2.1 Surface Plasmon Polariton (SPP)

Since both LSFL and HSFL orientation always depends on the polarization direction it can be inferred that they originate from an electromagnetic leading to a spatially modulated deposition (absorption) of the laser pulse energy. The absorption channels, however, can be different among the material classes. Usually, the excitation and interference of the Surface Plasmon Polaritons with the incident laser beam are involved and eventually lead in the formation of LSFL.

An improved and widely accepted mechanism that accounts for LSFL formation is further developed and depicted in the following equation:

$$\Lambda = \frac{\lambda}{\frac{\lambda}{\lambda_{spp}} \pm \sin \theta} \quad \text{Eq.2}$$

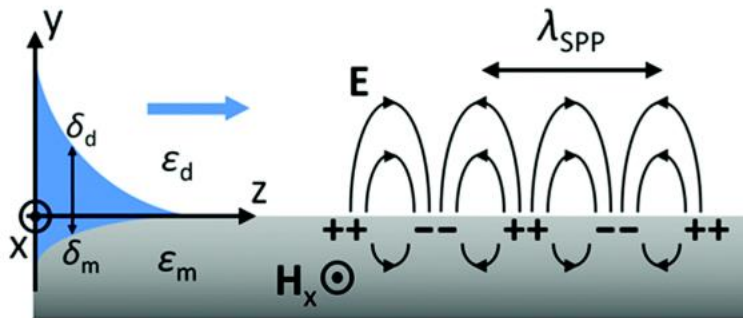


Figure 1.2: Illustration of the surface plasmon electromagnetic wave polariton, which propagates at the dielectric-metal interface. The +, - correspond to areas with a lower and a higher density of free electrons respectively, between which electric fields are created. The curves correspond to dynamic lines of the electric fields inside and outside the metal. Electric fields of the surface plasmons decay exponentially away from the interface, as shown left of the figure with their intensity show in blue.

The proposed mechanism relates the ripples generation to surface plasmon waves, considering that all solid surfaces show metallic behavior at high temperatures allowing excitation of surface plasmon waves. Such waves are electron density waves propagating at the interface between a metal and a dielectric and are often called surface plasmon polaritons (SPP). SPP, can be defined as the coupling of the surface plasmon and the electric field of the laser beam; it can be generated during the material irradiation due to the accumulation of free carriers.

In principle, all the previously mentioned laser beam parameters (wavelength, pulse duration, fluence, number of pulses, angle of incidence, and beam polarization state) determine the onset of the surface modification as energy absorption, electrodynamical effects and relaxation processes are critical to the material heating. Femtosecond laser interaction also involves several complex phenomena, including energy absorption, photo-ionization processes, electron excitation and electron-relaxation processes.

Like every material, when we perform excitation using high intensity and number of pulses, due to the defects surface waves are created. There are two types of surface waves: far field and near field. Far field waves result in the formation of LSFL, while near field waves result in HSFL ripples. The surface waves direction depends on the optical properties of the material, solving the Maxwell equations. For metals ($R_e(n) < 0$), the direction of far fields is parallel to the polarization, forming perpendicular LIPSS. In the case of dielectrics ($R_e(n) > 0$), like polymers, the direction of far fields is perpendicular to the polarization, forming parallel LIPSS. For near field waves the outcome is the opposite in both cases.

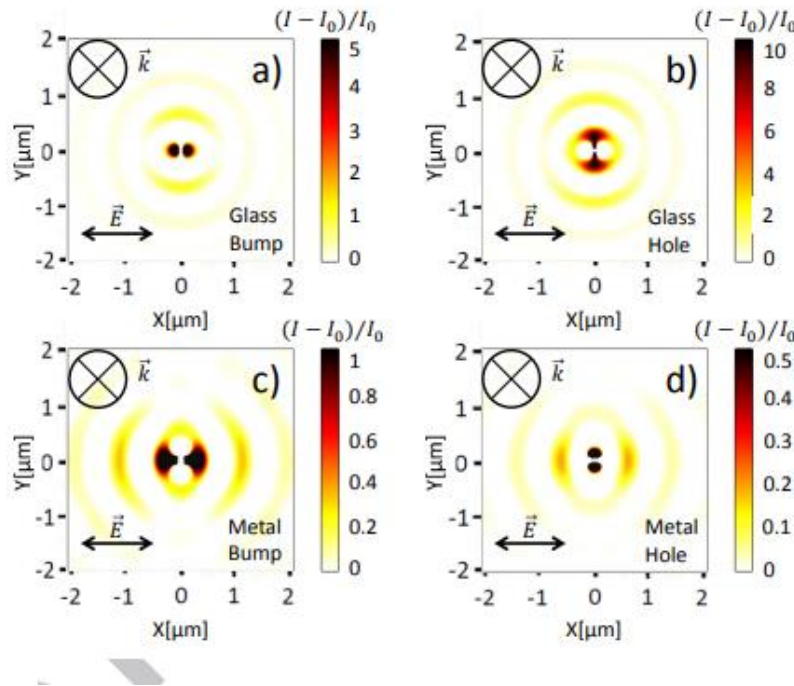


Figure 1.3: Absorbed energy in the transverse plane on glass surface with (a) a bump, (b) a hole and on metal surface with (c) a bump, (d) a hole of $R = 20$ nm. Light interaction exhibits contrasting polarization-sensitive interference patterns (in the micrometer scale) depending on the optical material properties and the nature of imperfections.

1.2.2 Interference of surface plasmon with the laser beam

The phenomenon of the interaction of the laser beam with the matter that analyzed previously, i.e., the surface plasmon polariton wave propagating at the metal-dielectric interface is responsible for the generation of ripples.

Surface plasmons contribute to the incident vertical beam of the laser and the form an amplifying interference fringe with vector $G = K_i - K_s$, where $K_i = \frac{2\pi}{\lambda}$ is the wavevector of the laser beam, $K_s = \frac{2\pi}{\lambda_s}$ is wavevector of the surface plasmons and $G = \frac{2\pi}{\Lambda}$. From these equations, it is important to clarify the different wavelengths, so, λ denotes the wavelength of the laser beam, λ_s corresponds to the wavelength of the surface plasmons, and Λ is the period of the wave structures.

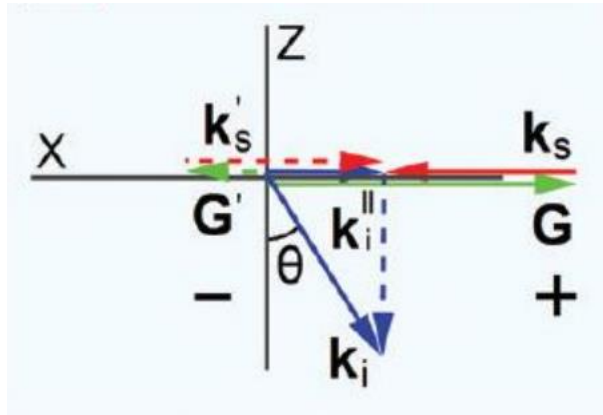


Figure 1.4: Wavevector imaging of the contribution of the laser beam k_i to the surface plasmon k_s for the formation of the surface plasmon polariton G .

Considering the analysis at the interface it follows that the period of the structures Λ is calculated by the formula $\Lambda = \frac{\lambda}{\frac{\lambda}{\lambda_s} \pm \sin\theta}$, where θ is the angle of incidence of the laser beam.

The real part of the dielectric function for metals is smaller than -1 ($\epsilon' < -1$) for the generation of surface plasmons, while for polymers the dielectric properties depend upon their structure which determines whether a polymer is polar or non-polar and this in turn decided the electrical properties of the polymer. The dielectric constant of most polymers the dielectric constant $\epsilon \approx 2$.

1.2.3 Two Temperature Model

To determine the temperatures involved in the formation of fs-LIPPS, a two-temperature model (TTM) has been proposed. In this model, electrons and lattice subsystems are described separately by their own temperature distribution. The electronic temperature is estimated assuming that the laser energy is first transferred to the electrons, and then the lattice temperature is determined by assuming energy transfer from the electrons to the lattice. This model has been mainly used to simulate the interaction of short pulses with metals but has also been applied to other materials such as silicon. However, the strong non-equilibrium conditions associated with ultrashort pulsed laser interaction with solids makes a detailed theoretical

analysis difficult. In the case of soft materials, such as polymers, numerical simulations of the evolution of temperature distribution on the surface and within the bulk have also been reported, considering again the generation of free electrons.

TTM has been widely used with a lot of variations depending on the materials and the irradiations to calculate the temperature variations between the electron and lattice subsystems. Due to the fact that the beam spot diameter typically varies from 10-100 μm , greater than the optical-electron penetration depth the energy transport into a metal can be described by the following one-dimensional two temperature diffusion model. Hence assuming that the electron thermalization is very fast and that the electron-lattice temperatures can be described by T_e and T_l .

Evolution of electron temperature in time:

$$C_e \frac{\partial T_e}{\partial t} = -\frac{\partial Q(z)}{\partial z} - \gamma (T_e - T_l) + S$$

Evolution of lattice temperature in time:

$$C_l \frac{\partial T_l}{\partial t} = \gamma (T_e - T_l)$$

Heat flux:

$$Q(z) = -k_e \frac{\partial T_e}{\partial z}$$

Laser heating source:

$$S = I(t) \cdot A a e^{-az}$$

Where z axis is always perpendicular to the target surface, $Q(z)$ the heat flux, S is the laser heating source. $I(t)$ is the laser intensity, $A = 1 - R$ and R the reflectivity, a are the surface transmissivity and the materials absorption coefficient. C_e, C_l are the heat capacities for the electron and lattice subsystems and γ is the electron phonon coupling parameter which can be expressed as $\gamma = \frac{C_e}{\tau_e}$, where τ_e stands for the electron, lattice characteristic heating phases, for every case.

1.2.3.1 TTM and femtosecond laser pulses

In this thesis we conduct all our experiments with laser pulses of duration of some tens of femtoseconds. The use of laser pulses at the fs-regime is preferred in order to not only to provoke surface morphological changes but also to avoid as much as possible the pronounced thermalization that laser irradiation can cause to the surface. The total energy deposition is finished before the excited electron system starts to return (relaxation) on ground state and eventually reach thermal equilibrium. Therefore, we must consider that the pulse duration (τ_p) is less in time than the electron cooling time. In our case the pulse duration is shorter

than the electron cooling time ($\tau_p \ll \tau_e$) as we irradiate with ~ 170 fs pulse duration. So, this means that for $t \ll \tau_e$, the $\frac{C_e}{T_e} \gg \gamma T_e$, the electron-lattice coupling can be neglected. The electron temperature can be calculated as following: $C'_e \frac{\partial T_e^2}{\partial t} = 2(1-R)I(t)a e^{-az}$.

Assuming that the laser intensity I and the material reflectivity R , are constant in time: $T_e(t) = \sqrt{T_0^2 + \frac{1I_a a}{C'_e} \cdot e^{-az}}$, where $I_a = I_0 A$, with I_0 constant, and $T_0 = T_e(0)$ as the initial temperature.

Finally, as the end of the laser pulse (as $T_0 \ll T_e$): $T_e(\tau_p) \approx \sqrt{\frac{2I_a \tau_p a}{C'_e} \cdot e^{-az}}$.

1.2.3.2 Combined TTM and Hydrodynamic effects

In 2012 Tsibidis and colleagues introduced a unifying theoretical framework by considering that hydrodynamic, and not mass removal, effects constitute the main agent that govern the initial morphological changes. The combined theory can provide an extension based on the spatial dependence of the laser intensity distribution that induced bending of the isothermal lines. The proposed model comprises, a heat transfer component that accounts for the particle dynamics and heat conduction phenomena and a hydrodynamics component, which describes the molten material dynamics and the resolidification process.

In this context considering a Newtonian incompressible fluid for the mass conservation $\vec{\nabla} \cdot \vec{u} = 0$, where \vec{u} is the velocity of the fluid while for the energy conservation:

$$C_l \left(\frac{\partial T_l}{\partial t} + \vec{\nabla} \cdot (\vec{u} T_l) \right) = \vec{\nabla} \cdot (K_l \vec{\nabla} T_l)$$

And for the momentum conservation:

$$\rho_l \left(\frac{\partial \vec{u}}{\partial t} + \vec{\nabla} \vec{u} \cdot \vec{u} \right) = \vec{\nabla} \cdot (-P + \mu (\vec{\nabla} \vec{u}) + \mu (\vec{\nabla} \vec{u})^T)$$

Where K_L is the thermal conductivity of the lattice, μ is the liquid viscosity, P pressure, and K_L stand for the thermal conductivity of the liquid phase, respectively. It is evident that the transition between a purely solid to a completely liquid phase requires the presence of an intermediate zone that contains material in both phases.

Although, the two-temperature model is an established model to describe the interference and formation of LIPSS, in the case of polymers it isn't the answer to the theoretical aspect. That is because polymers are non-organized structures and the T_e value can't be found. Also, the nature of polymers changes completely after laser irradiation. Until now there is no model that can describe laser induced-periodic surfaces on polymers and because of its nature and difficulties this matter is concerned to be a very tricky one.

1.3.3 Dependence of periodicity on the number of the laser pulses

In this section it will be described how the periodicity of wave structures form the number of pulses incident through stationary radiation at a point. Due to the Gaussian distribution, at a large number of pulses, there will be no structures in the center of the point, so for the following proof we use the periodicity at the periphery of the point.

The period of structures at the periphery of the irradiated spot is related to the diameter of its crater. This phenomenon is due to the gaussian distribution of the beam, at the focal distance, The Gaussian distribution is a curve where the maximum intensity value is located at its peak. In detail, with the increase in the number of the pulses, this diameter increases because the spot becomes more and more saturated. By increasing the diameter of the crater, the area of the periphery decreases because the beam has a fixed diameter, Thus, for constant energy density, it is observed that as its diameter increases crater there will be less and less energy density distributed in the periphery and correspondingly increasing energy density in the center. Then, the decrease in energy density in the periphery excites a smaller percentage of electron density of the periphery. The electron density is proportional to the energy density and has a Gaussian distribution.

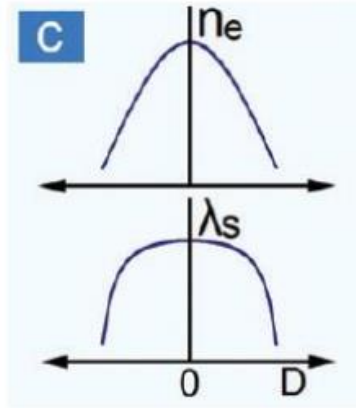


Figure 1.5: From the Gaussian distribution of beam electric fields the n_e or n and λ_s or λ_{sp} , is reduced by center to the edges of the irradiated spot.

Furthermore, knowing that the electron density, n , is the no of valence electrons per volume ($n = \frac{N}{V}$) and using the plasmon angular frequency equation, we conclude that as the electron density decreases, the plasmon frequency also decreases. This directly affects the real part of the dielectric function. According to the relation, the reduction of the absolute value of the plasmon frequency leads to the reduction of the absolute value of the real part of the dielectric function, which in turn reduces the wavelength of the surface plasmon. Finally, as through radiation at a vertical angle $\Lambda = \lambda_{sp}$ is valid, we can state the theoretical approach that increasing the number of the pulses leads to a reduction in the period of the wave structures.

$$\omega_p = \sqrt{\frac{4\pi e^2 N}{m}} \rightarrow \omega_p = \sqrt{\frac{4\pi e^2 n v}{m}}$$

$$|\varepsilon'_1| = \left| 1 - \frac{\omega_p^2}{\omega^2} \right| \quad \lambda_{sp} = \lambda \sqrt{\frac{\varepsilon' + \varepsilon_d}{\varepsilon' \cdot \varepsilon_d}}$$

Chapter 2: Light Polarization

The electromagnetic wave of the beam radiated by a laser source, consists of two components, the electric field \vec{E} and the magnetic field \vec{M} . These two components are perpendicular to each other and perpendicular to the direction of wave propagation.

The polarization is defined by the direction of the electric field \vec{E} , which is perpendicular to the propagation of the wave. Depending on the direction of the electric field, different types of polarization result:

- Linear polarization: The direction of the electric field is fixed, that is, the electric field of the beam oscillates in only one direction during wave propagation. Every linearly polarized wave that propagates along an x-axis, can be resolved into two linear polarized components \vec{E}_z and \vec{E}_y . The cases of linear polarization can be distinguished:
 - Vertical linearly polarized beam, which propagates to y-axis ($\vec{E}_z = 0$)
 - Horizontally linearly polarized beam, which propagates to z-axis ($\vec{E}_y = 0$)
 - Linearly polarized beam with random direction. It arises from vertically and horizontally polarized beam composition, these are sufficient have the same frequency and no phase difference

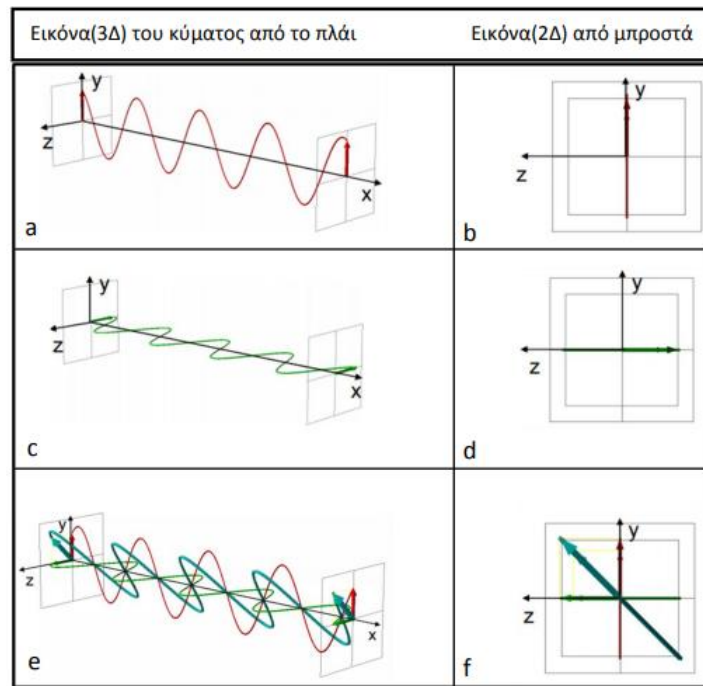


Figure 2.1: The direction of oscillation of the electric field vector for the different linear polarizations. Images a-b correspond to vertical linear polarization, c-d to linear polarization and e-f to linearly polarized beam in random direction.

- Radial polarization: The direction of the electric field is constant. The electric field is constant. The electric field \vec{E} of the beam is symmetric and at every instant of time is directed radially, leaving the center of the beam unaffected. To create such a polarization a s-waveplate is used, which is a

glass irradiated with fs pulses, which converts the linearly polarized Gaussian in radially polarized cylindrical beam.

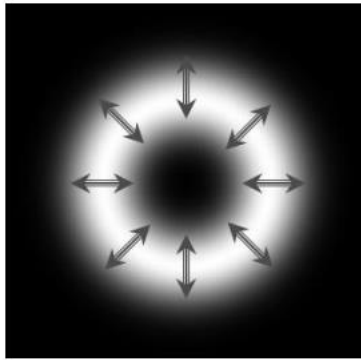


Figure 2.2: Electric field distribution of the radially polarized cylindrical beam (assuming beam propagation perpendicular to the plane).

Chapter 3: Experimental methods and analysis

The direct fabrication of LIPPS structures is based on laser matter interactions with specific parameters. The effects that lead to the desired laser structuring are performed under certain conditions of the laser beam parameters such as wavelength, pulse duration and energy, beam size, polarization and repetition rate. In this chapter, the experimental methods including the definition of the laser beam parameters, instrumentation such as laser type, optics, material targets, electronics and mechanical devices are presented.

3.1 Laser beam spatial profile

The Gaussian intensity profile is the most common laser beam mode, and it can be described as a fundamental transverse electromagnetic mode. This Gaussian mode describes the intended output of the most commercial laser, given that such beam can be focused into the most concentrated spot. For a Gaussian beam, the spatial profile of the normalized pulse fluence $F(r)$ along the diameter of the beam r , is given by:

$$F(r) = \frac{2 E_p}{\pi w_0^2} \cdot e^{-\frac{2r^2}{w_0^2}}$$

Where E_p is the pulse energy and w_0 the waist of the fundamental Gaussian beam. The maximum fluence value occurring within the Gaussian profile when the radius $r = 0$, is commonly named as peak fluence F_p :

$$F_p = \frac{2E_p}{\pi w_0^2}$$

The spot size or beam waist of a Gaussian beam is the location along the beam axis where the intensity is $\frac{1}{e^2}$ its own maximum value. A simple method to measure the spot size of the Gaussian beam is to use the fabricated circular craters produced by amorphization or ablation was provided in 1982 by Liu. Considering the actual laser damaged craters radius profiles r_a (*vertical radius*) and r_b (*horizontal radius*) and plotting out the following relations:

$$E_a = E_p \cdot e^{-\frac{2r_a^2}{w_0^2}} \quad E_b = E_p \cdot e^{-\frac{2r_b^2}{w_0^2}}$$

We end up with the extracted dependence of r_a and r_b as:

$$r_a^2 = \frac{w_0^2}{2} \ln \left(\frac{E_p}{E_a} \right)$$
$$r_b^2 = \frac{w_0^2}{2} \ln \left(\frac{E_p}{E_b} \right)$$

We can also calculate the threshold fluence value: $F_{th} = \frac{2E_{a,b}}{\pi w_0^2}$

Additionally, the beam w_0 can be calculated theoretically. The theoretical beam radius of a collimated laser beam after passing through the focusing (converging) lens calculated by the following equation

$$w_0 = \frac{(2f\lambda M^2)}{\pi D}$$

Where f is the focal length of the focusing lens, λ is wavelength of the laser, D is the input/collimated laser beam diameter onto the focusing lens, and M^2 is the beam propagation factor, which describes the difference between a real laser beam and an ideal diffraction-limited Gaussian beam.

3.2 S-Waveplate polarization converter

To convert polarization from linear to a complex state, we can use several segments of $\lambda/2$ phase waveplates with different discrete crystal layers. Such a converter was utilized to convert our laser typical Gaussian and linearly polarizer beam to a doughnut shaped cylindrically polarizer beam. This polarization converter is an s-waveplate and the most fascinating aspect of it that it works using nanograting HSFL structures. Continuous phase profiles of nearly any optical component can be fabricated in silica, which allows unparalleled control over the local phase of a laser beam that is transmitted by element.

For the incident circular-polarized beam, the radial or azimuthal polarization can be formed with a space variant quarter-wave plate possessing a radial symmetry, which can be described using Jones calculus with the following matrix:

$$\begin{pmatrix} \cos^2\theta + i \sin^2\theta & (1-i) \cos\theta \sin\theta \\ (1-i) \cos\theta \sin\theta & i \cos^2\theta + \sin^2\theta \end{pmatrix}$$

Where angle $\theta = \psi + \frac{\pi}{4}$ and ψ is a polar angle. Multiplying a vector describing the left-handed circular polarization by this matrix the following expression is derived:

$$\begin{pmatrix} \cos^2\theta + i \sin^2\theta & (1-i) \cos\theta \sin\theta \\ (1-i) \cos\theta \sin\theta & i \cos^2\theta + \sin^2\theta \end{pmatrix} \frac{1}{\sqrt{2}} \begin{pmatrix} 1 \\ i \end{pmatrix} = \begin{pmatrix} -\sin\psi \\ \cos\psi \end{pmatrix} e^{i\psi} e^{\frac{i\pi}{4}}$$

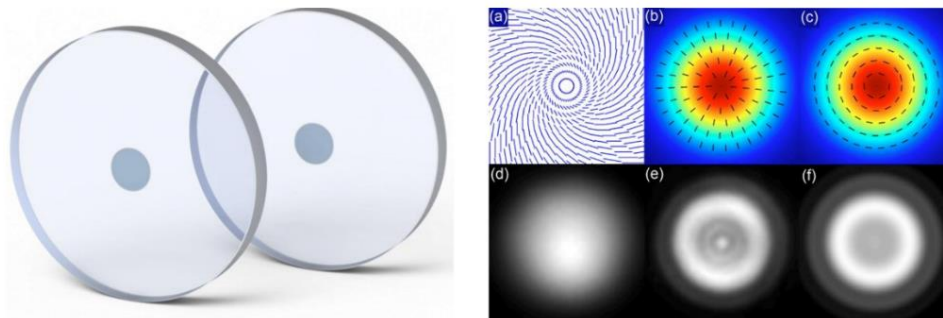


Figure 3.1: Actual image of the commercial optical element (on the left), image reprinted from www.altechna.com. On the right, color online (a) Schematic drawing of nanograting distribution in polarization converter. (b) and (c) Distribution of the electric field for left-hand and right-hand circularly polarized beams (see white circles) polarized beam after passing through the polarization converter. (d) and (e) Measured beam profiles before and after beam converter. (f) Modeled beam profile after beam converter. Image reprinted from ref

This enables fabrication of advanced optical components (like q-plates) that can generate beams with radial and azimuthal polarization. The s-waveplate can operate as polarizing retarder without the capability for any degree of freedom regarding the polarization conversion, but with much higher laser damage thresholds.

3.3 Laser system - Experimental set up

All the experiments of this thesis took place in the laboratory ultrafast micro and nano processing at ITE-IHDL, using the system Pharos laser. This system emits a beam with a wavelength of 1026 nm and supports a second harmonic beam with a wavelength of 513 nm, a third harmonic of 342 nm and a fourth harmonic of 257 nm. The maximum Pulse Energy is 1.5 mJ and the Repetition Rate that can be adjusted by the system ranges from 1 kHz to 200 kHz. The pulse duration can take values from 170 fs to 10 ps. However, to observe morphological changes and self-organized structures on the surface of the polymer, the shortest possible pulse duration is preferred.

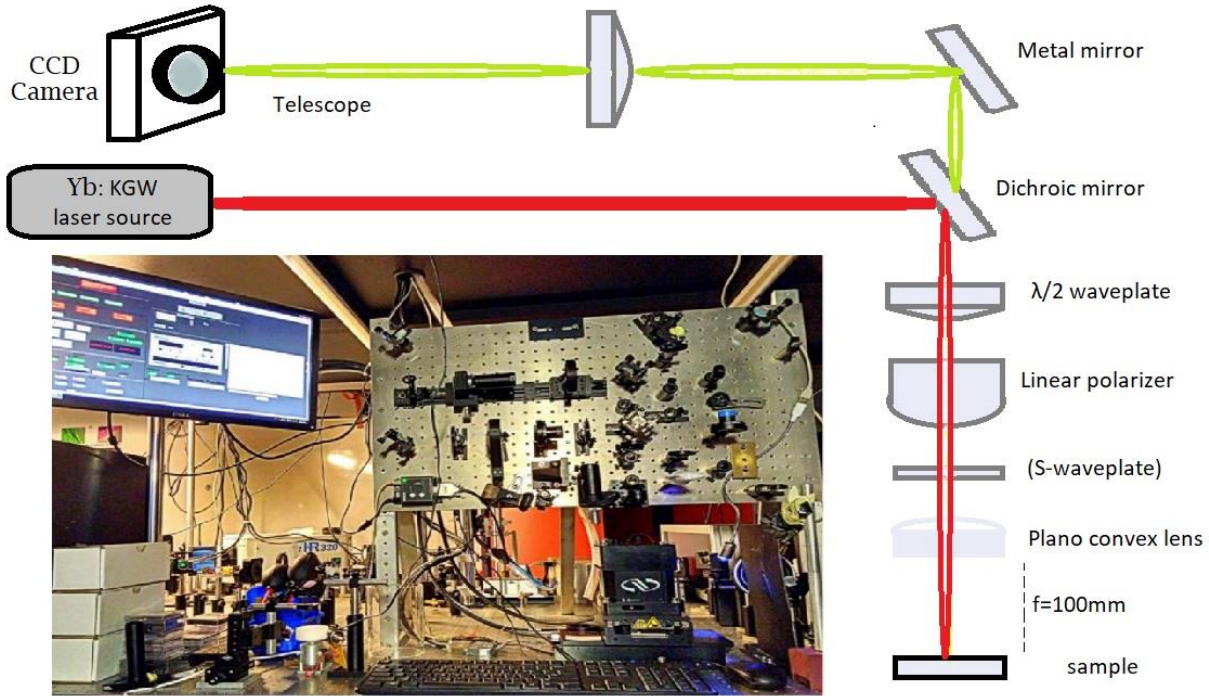


Figure 3.2: Photograph and schematic representation of the experimental set up developed and used to conduct all the experimental procedures on this thesis. The beam profiles for both Gaussian and CV beam are presented on the left.

In all the thesis experiments the laser pulses were focused on each sample via plano convex lens of 100 mm focal length while the Gaussian and (CV) spot diameter, measured by a CMOS camera within the Rayleigh length of the focal plane at $1/e^2$, was $\sim 49\mu\text{m}$ diameter for the IR and $\sim 27\mu\text{m}$ for the second harmonic. All The samples were mounted onto a 3-axis motorized servo stage from Newport and positioned perpendicular to the incident beam. A CCD camera mounted above the sample were used visualize in situ all experimental process on the sample surfaces. While all the irradiations were performed in ambient environment at normal incidence (~ 90 degrees). At the same time, power modulation was achieved by means of an automatically rotating zero-order half wave plate behind a high extinction ratio (10000:1), glan-taylor linear polarizer.

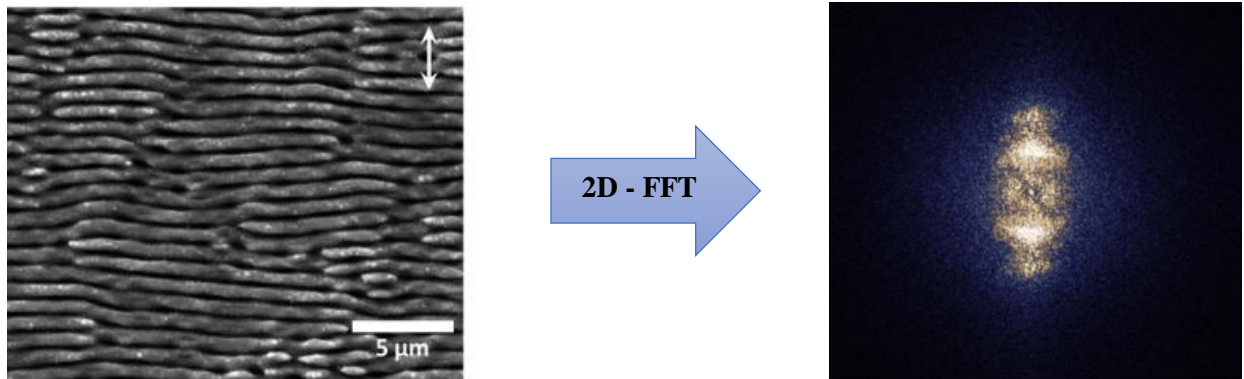
3.4 Characterization methods

3.4.1 Period measurements & Fourier analysis

To characterize the laser fabricated LIPSS structures, besides monitoring its geometry and shape, the LIPSS periodicity and topography and its respective dispersion should be accurately estimated. For this purpose, the scanning electron microscopy (SEM) and (AFM) images of the irradiated surfaces were examined through image analysis software such as ImageJ and Gwyddion and in most cases static measurements were performed for the best possible approximation of the surface morphological features. The exact procedure of the transformation and subsequent analysis is presented below.

Two-dimensional fast Fourier transform surface image analysis

In order to be able to extract frequency information a 2D fast Fourier transform (2D-FFT) transform was employed. High-resolution (1280x1024) SEM pictures had been transformed in reverse space images via a 2D-FFT algorithm. The new dimensions of the generated Fourier images are inversely proportional to x and y dimensions of the original image.



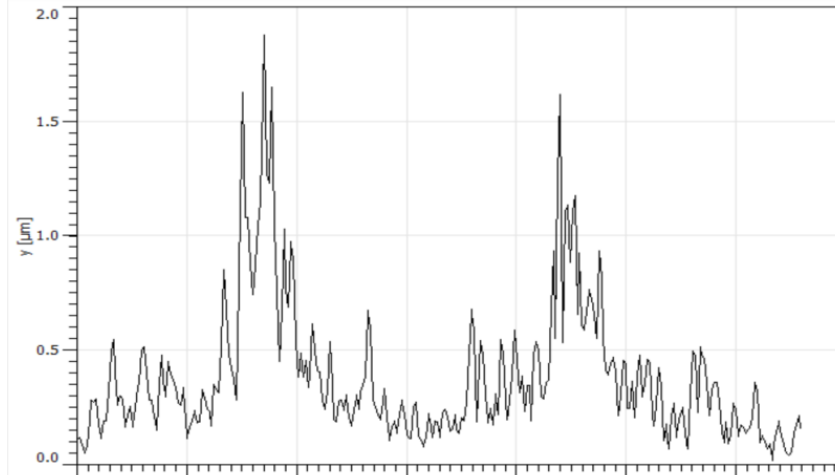


Figure 3.3: SEM images of stainless steel. In the third photo we can see the two peaks that correspond on the intensity of the attained characteristic frequencies in the Fourier space.

Along this direction the Fourier detects periodical fluctuation of the frequency intensity. This fluctuation exhibits an average frequency which is inversely proportional to the average ripple period. More specifically, the first peak represents the characteristic frequency f of the periodic structure. To calculate the periodicity, Λ , of the structures first we calculate the average frequency of each peak for a vertical as well as horizontal image cross section, and the average period is given by the relation $\langle \Lambda \rangle = 1/f$.

For the estimation of range of frequencies involved into the respective 2D-FFT images, we applied a Lorentzian Fit on both peaks of the cross section and the error of each measurement is calculated using the relation: $\Delta \Lambda = \left| -\frac{1}{f^2} \right| \cdot \Delta f$, where Δf is the mean of the linewidths for two Lorentzian of the 2D-FFT image profile peaks.

3.4.2 Characterization techniques

There are various characterization methods and instruments used for optical, morphological, topographical, and chemical analysis. Those that have been in this thesis are presented in the table below (Table 1). For the morphological characterization we use different techniques including optical microscopy (OM), scanning electron microscopy (SEM), atomic force microscopy (AFM), depending on any specific experiment. Furthermore, techniques such as UV-Vis spectroscopy, Fourier-transform infrared spectroscopy (FTIR), Ultraviolet-visible spectroscopy (UV-VIS) were used for optical characterization and Energy-dispersive X-ray spectroscopy (EDX) were available and used to collect more information on phase study and elemental analysis when appropriate. Another important measurement is that of the contact angle where liquid (water) is dropped to the irradiated surface, and we measure the angle that molds to make inference for the surface wettability and characterize it as hydrophobic or hydrophilic.

Operation	Instrument	Observation	Details
Surface analysis	Atomic Force Microscopy (AFM)	Surface Morphology and Topography	Microscope with piezo scanner J working in

			tapping mode, using sharp tips
	Optical Microscopy	Surface imaging (resolution≤100x)	Leica DC2700 M
	Field Emission Scanning Electron Microscope (FESEM)	Surface Morphology	JEOL 7000F with Shottky field-emission electron gun and secondary electron detector. (x10 ≤ magnification ≤ 650000)
Spectroscopy	Ultraviolet-visible spectroscopy (UV-VIS)	Optical Characterization	PerkinElmer Lambda 950 UV-VIS lamda 950 spectrometer with an integration sphere
	Fourier-transform infrared spectroscopy (FT-IR)	Polarization Response in the IR – Mid-IR	Bruker Vertex 70v FT-IR vacuum spectrometer, in a spectral range of 1.33-28.6 μm
Wettability of materials	Contact angle measurement	θ_c	

3.4.3 Pulse Calculation

The number of pulses that occur during irradiation is a very large important factor and should be determined in any kind of irradiation because it affects the morphology of the structure and most importantly the periodicity.

3.4.3.1 Static radiation

In the experimental arrangement of the laser a shutter was used, with which the irradiation time is regulated, so the number of pulses incident on the sample during the static irradiation to create spots is also controlled. In particular, the laser in all experiments was set at 1kHz (=1000 pulses/s). So setting the shutter for 100ms of static exposure will land 100 pulses on the spot.

3.4.3.2 Dynamic radiation

For the characterization of lines and surfaces, it is necessary to determine N_{eff} , i.e., the number of laser pulses per unit length or per unit area. For dynamic irradiation, the previous method does not apply because in this case the irradiation is done on the move and the number of pulses is affected by the speed and by the overlap between two consecutive lines when scanning surfaces.

For Gaussian beam with linear polarization:

In line-scanning (1D) irradiation, N_{eff} corresponds to the number of incident laser pulses along a length equal to the diameter (2R) of the beam.

$$N_{eff_{line}} = 2R \cdot \frac{f}{v}$$

On surface (2D), N_{eff} corresponds to numbers of laser pulses incident on a surface equal to the area of the beam (πR^2).

$$N_{eff_{area}} = \pi R^2 \cdot \frac{f}{v \cdot \delta}$$

Where R is the radius of the Gaussian beam, f is the rate of repetition (pulses/sec), v is the speed and d is the speed distance (mm) between two consecutive lines in construction of the surface.

3.4.4 Laser fluence calculation

Energy density $\left(\frac{J}{cm^2}\right)$ is defined as the energy of the beam incident on a surface equal to the area of the beam (πR^2 for a Gaussian beam). The energy (J) of the beam is determined by the average power (mW) to the repetition rate (kHz) of the pulse. For beam area, the area of the irradiated spot (surface spot area) multiplied by $(1 - e^{-2})$ is used, in order define some limits on the Gaussian curve of the beam and to get as much as possible the effective area of the average radiation intensity.

- Focal Spot Area = $(1 - e^{-2})$, surface spot area
- Laser Pulse Energy = (Average Power) / (Pulse Repetition Rate)

- Laser Fluence = 2 (Laser Pulse Energy) / (Focal Spot Area)

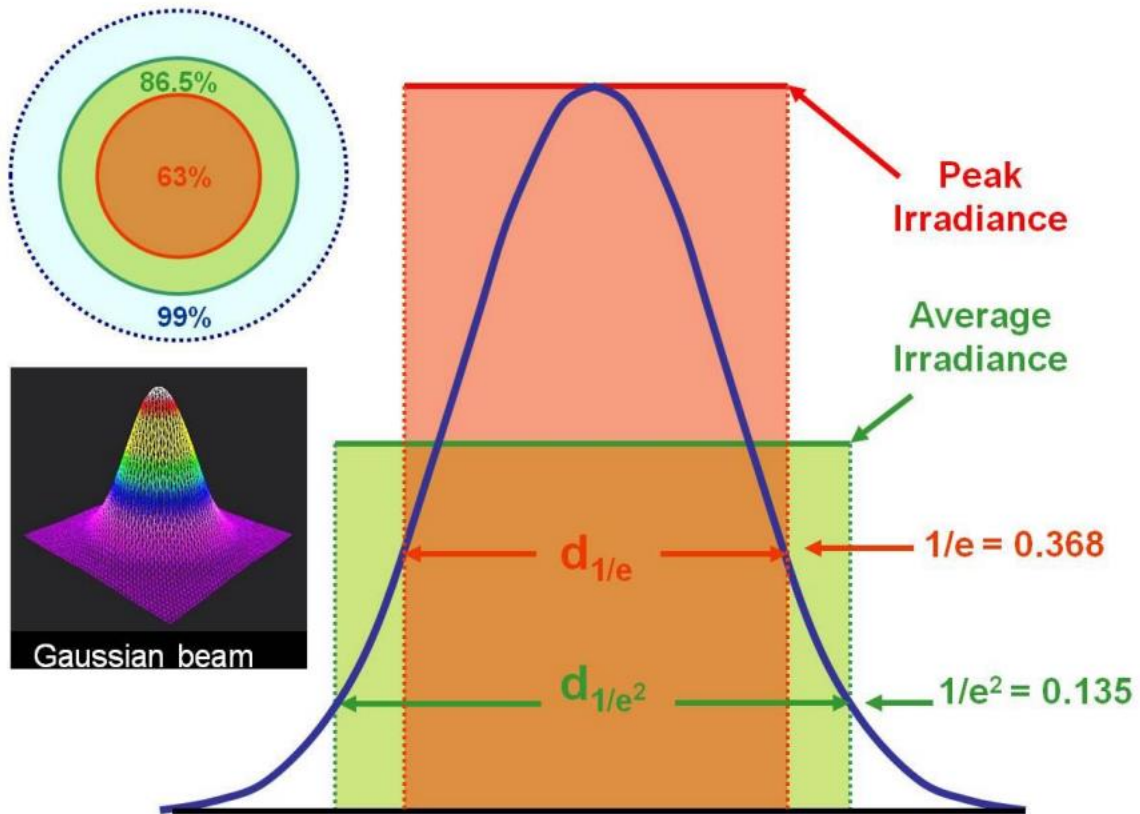


Figure 3.4: Plotting the Gaussian distribution of radiation intensity, delineating the edges of the curve that correspond to maximum and average intensity

In other words, the fluence value (F), is defined as:

$$F \left[\frac{J}{cm^2} \right] = \frac{E}{\pi \cdot \omega_0^2}$$

and describes the average energy per unit surface for a single pulse irradiation.

Chapter 4: Parametrical study

The purpose of the thesis is the treatment of a polymer surface through irradiation with linearly and circular polarized ultra-narrow laser pulses with the aim of creating surface periodic structures. The horizontal linearly polarized beam induced vertical wave-like structures in a single direction and the circular polarization dot-like surface structures. The wavelength of the laser used has a direct effect on the period of the structures. Using the laser's emission wavelength of 342nm, low-frequency wave-structures are formed 257nm

4.1 LIPPS Formation on Polycarbonate using 3rd harmonic and Analysis

First, the 3rd harmonic of the laser was used to study the structures that could be formed. The wavelength in this case is equal to 342nm and a morphological map of all the structures that were created is presented below.

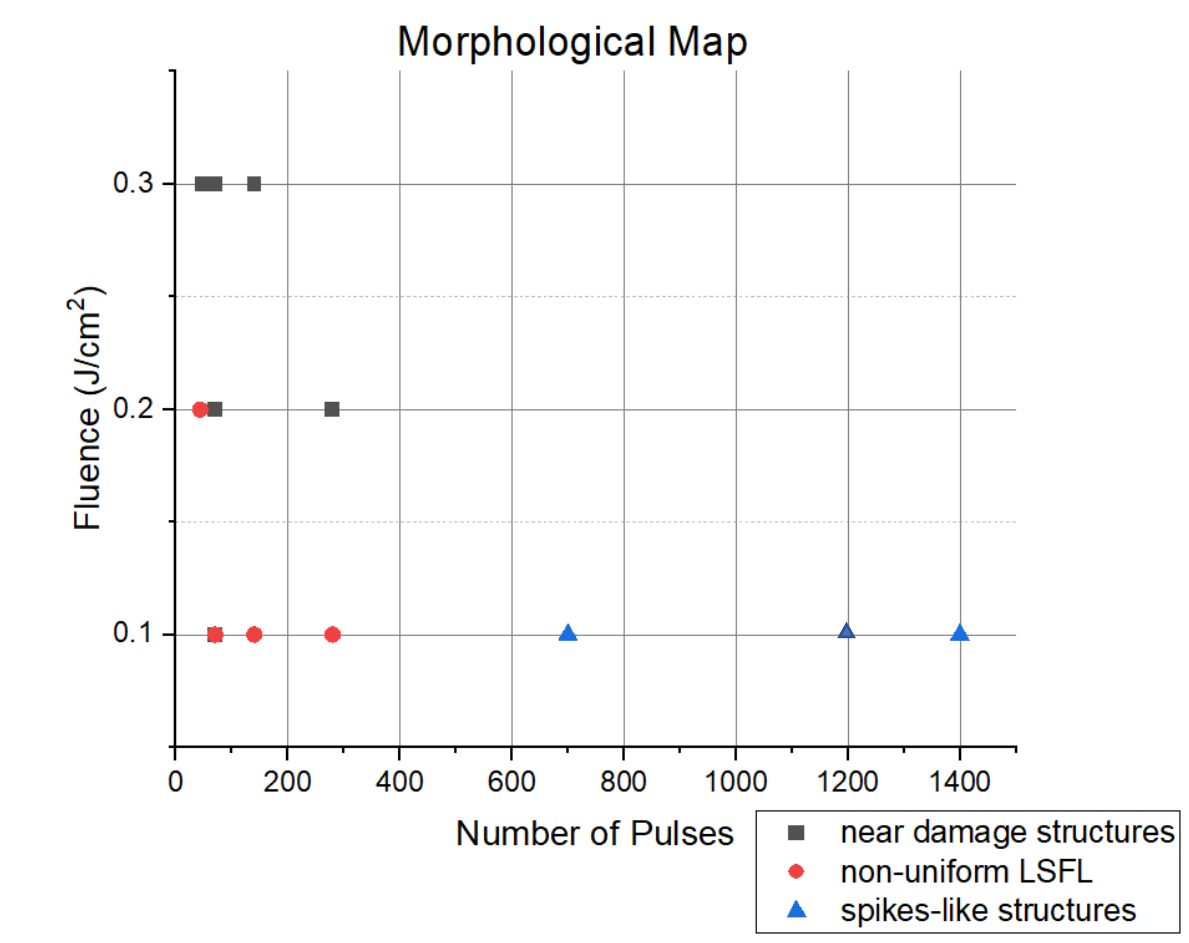


Chart 4.1: Morphological Map of structures using wavelength equal to 342nm and linear polarization in Polycarbonate material

The (*near*) *damage threshold structures* (presented with green color) stand for the following morphologies:

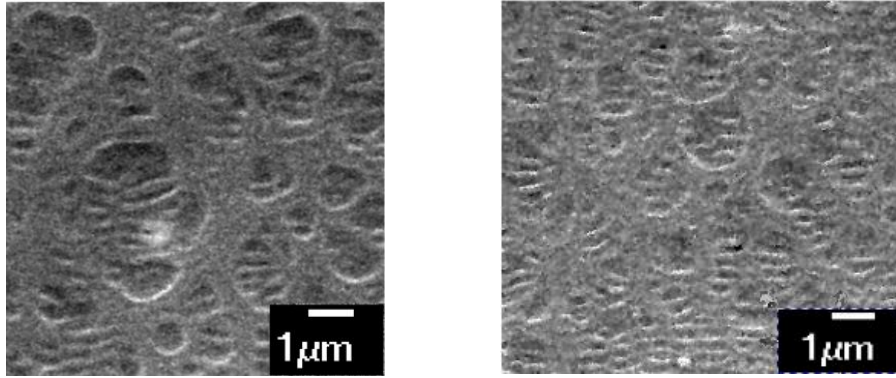


Figure 4.1: SEM pictures of damaged LSFL. Left: Fluence= 0.2 J/cm^2 , 70pps. Right: Fluence= 0.3 J/cm^2 , 70pps.

The *non-uniform LSFL* (presented with blue color) stand for the following morphologies:

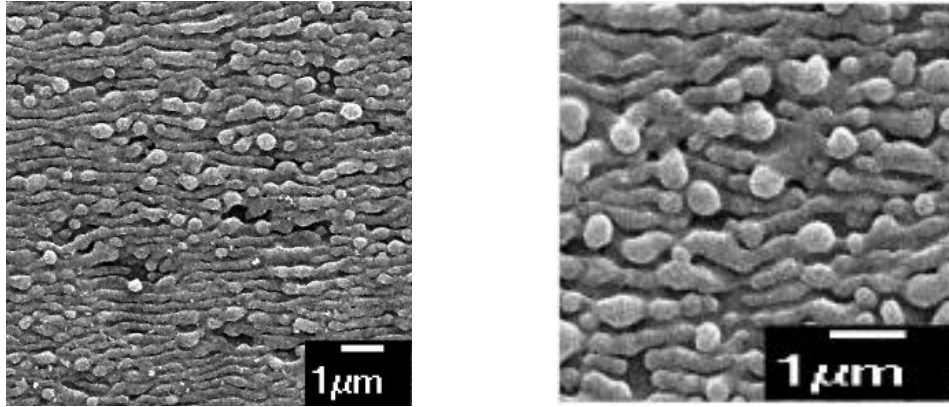


Figure 4.2: SEM pictures of non-uniform LSFL. Left: Fluence= 0.1 J/cm^2 , 280pps. Right: Fluence= 0.1 J/cm^2 , 70pps.

The *spikes-like structures* (presented with orange color) stand for the following morphologies:

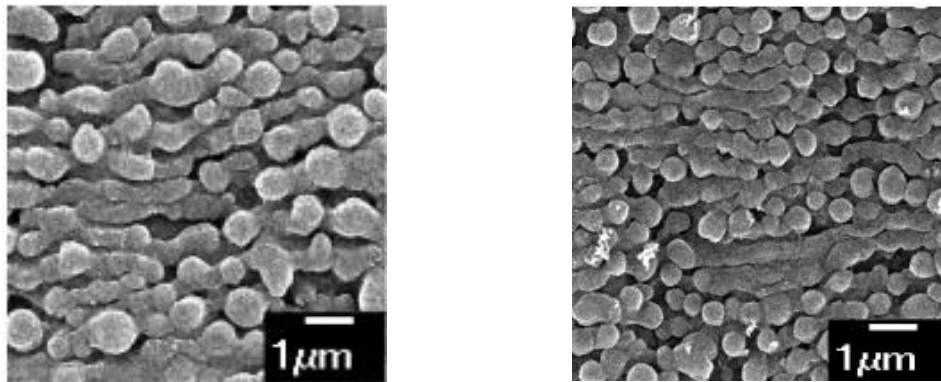


Figure 4.3: SEM pictures of spikes-like structures. Left: Fluence= 0.1 J/cm^2 , 700pps. Right: Fluence= 0.1 J/cm^2 , 1400pps.

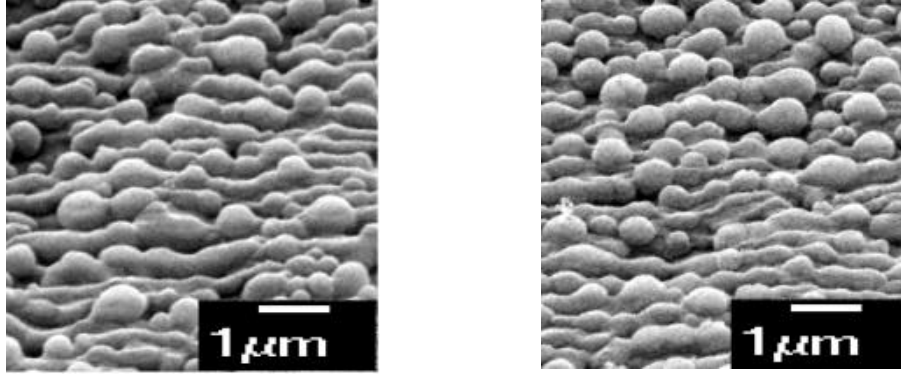


Figure 4.3: SEM tilted-view of spikes-like structures. Left: Fluence=0.1 J/cm², 700pps. Right: Fluence=0.1 J/cm², 1400pps.

We conclude that spikes-like structures appear for low Fluences and large number of pulses. The formation of these domes is not uniform, and their height is ~150nm. Generally, as fluence increases even for low number of pulses that structures are damaged. Furthermore, the non-uniform ripples that are formed are the transition between the damaged ripples and the spikes like. Uniform LSFL, as those we will study in the next paragraphs, were not observed.

Using the 2D-FTT transform, as explained previously, we calculated the Period for each of the periodical structures that were captured. Then, we made a chart of Periodicity over Number of Pulses, with fixed Fluence, both for the non-uniform LSFL and spikes-like structures, so that we would have a clear view of how periodicity behaves when changing the Number of Pulses in the material.

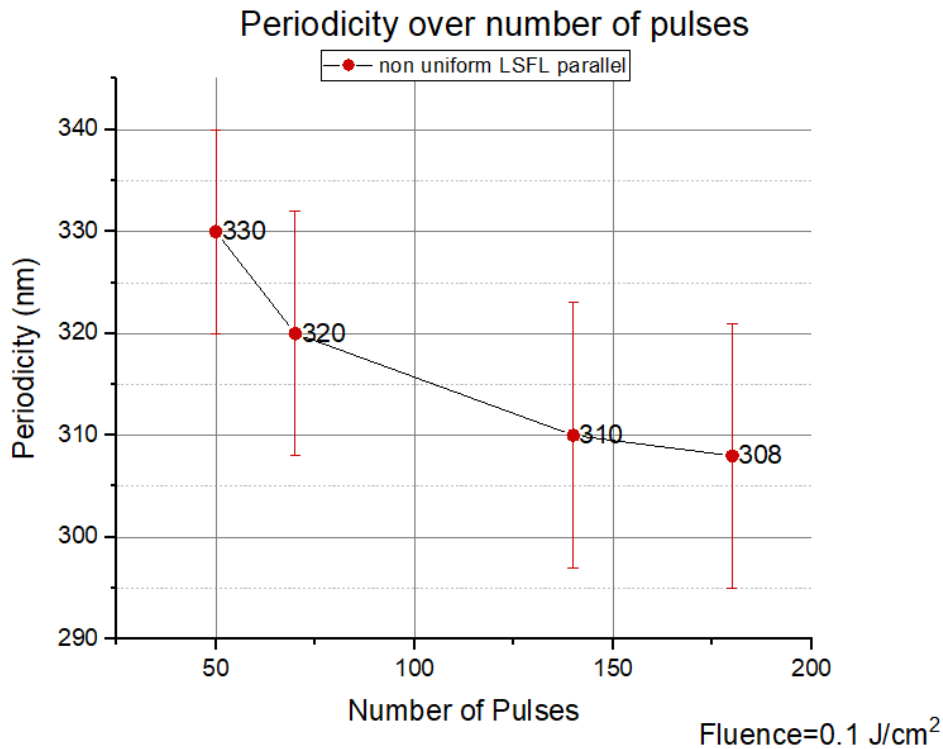


Chart 4.2: Periodicity over Number of Pulses chart, with constant Fluence=0.1 J/cm² for the non-uniform LSFL that were performed in Polycarbonate using 345nm wavelength (fs laser) and linear polarization.

As it is presented in the Chart 4.2, when increasing the number of pulses, the periodicity on the non-uniform LSFL, using 342nm, increases. We can see that the values appearing, are between the range of (308-330) nm, a little beat below the wavelength of our laser beam.

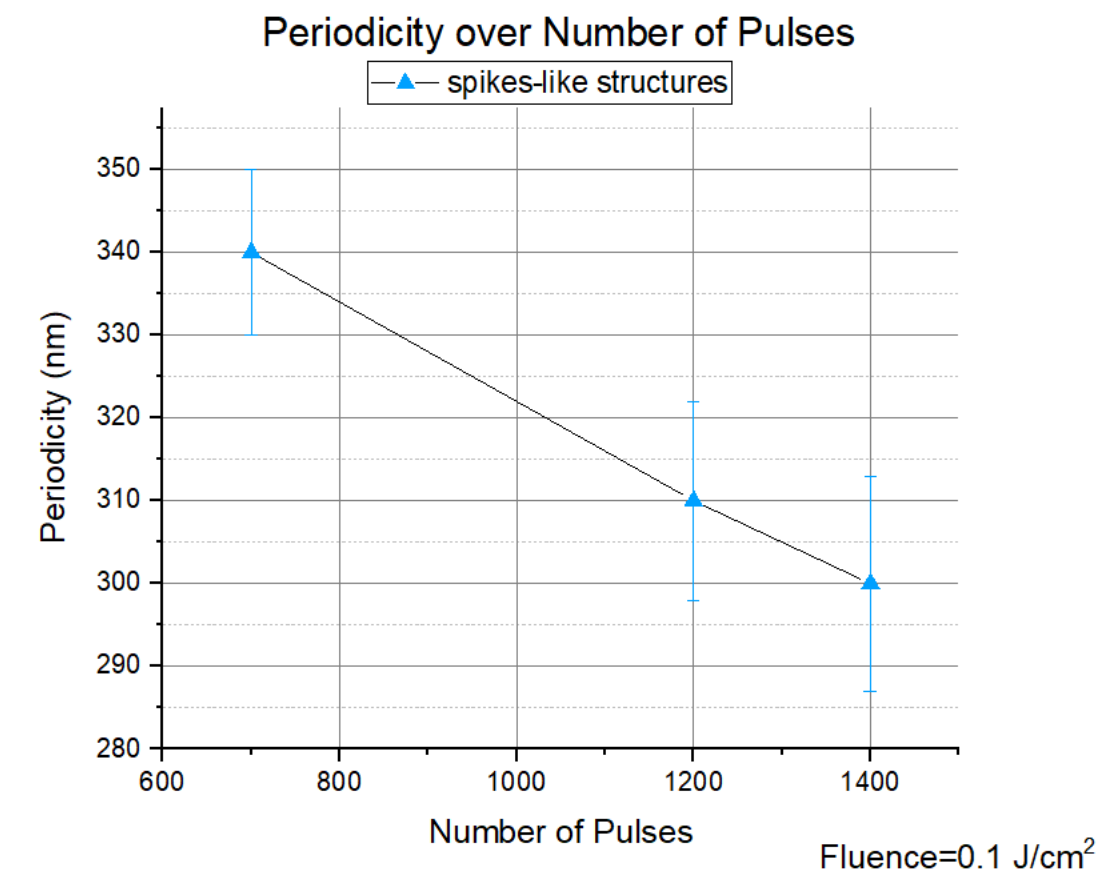


Chart 4.3: Periodicity over Number of Pulses chart, with constant Fluence=0.1 J/cm² for the spikes-like structures that were performed in Polycarbonate using 345nm wavelength (fs laser) and linear polarization.

In the same way we studied the spikes-like structures, setting a constant Fluence of 0.1 J/cm² (Chart 4.3). In this case we can see that as the number of pulses increases the periodicity of the structure's declines. However, we cannot have a clearer view, because of the small range that this morphology appears.

4.2 LIPPS Formation on Polycarbonate using 4th harmonic and Analysis

We then proceeded in using the 4th harmonic generation of the laser, to study the structures that could be formed, having linear polarization. The wavelength in this case is equal to 257 nm and a morphological map of all the structures that were created is presented below.

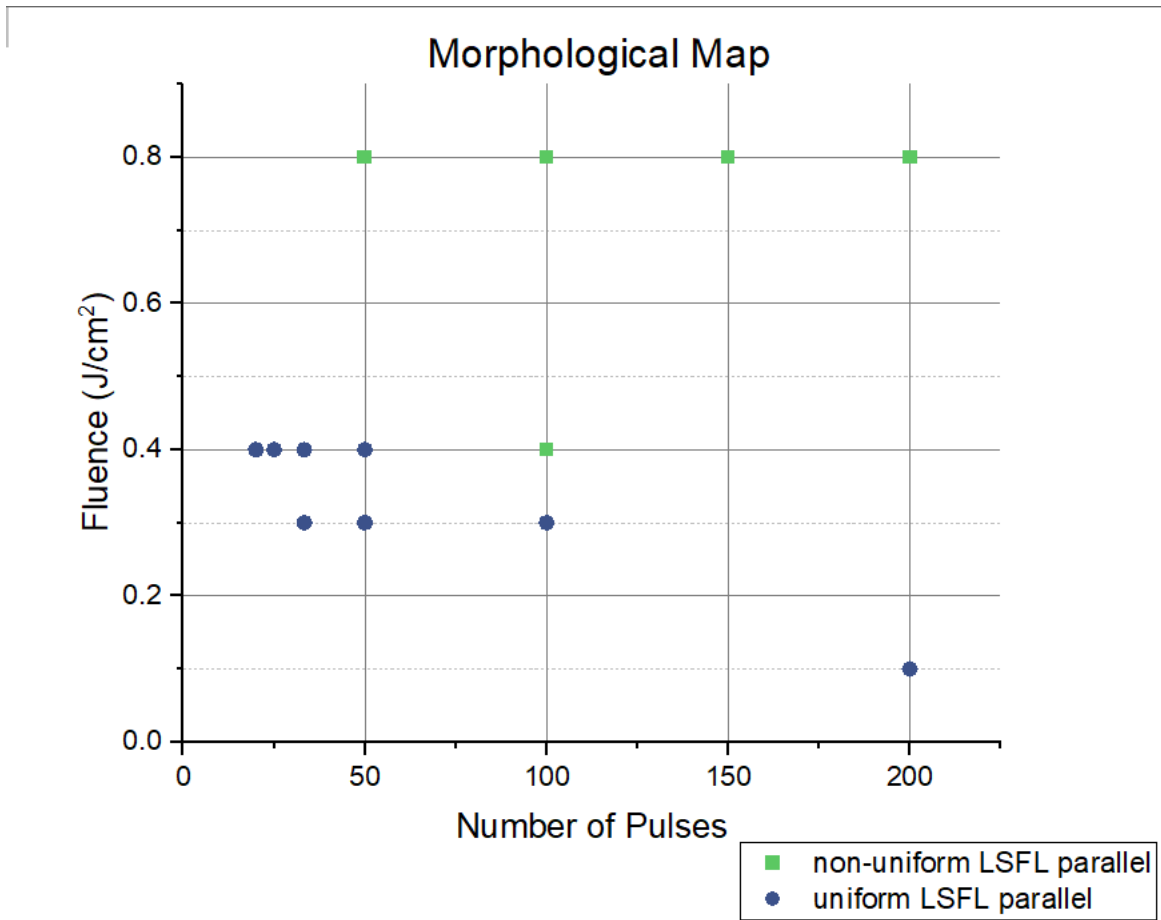


Chart 4.4: Morphological Map of structures using 257nm wavelength and linear polarization in Polycarbonate material.

The *non-uniform LSFL parallel* (presented with blue color) stand for the following morphologies:

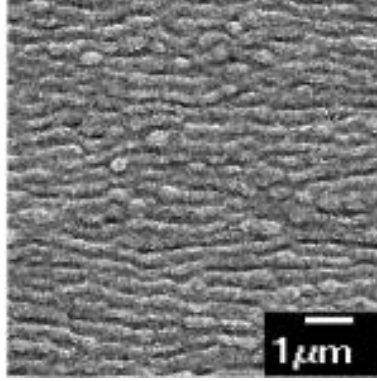


Figure 4.4: SEM pictures of non-uniform LSFL. Left: Fluence= 0.4 J/cm^2 , 100pps. Right: Fluence= 0.4 J/cm^2 , 10pps.

The *uniform LSFL parallel* (presented with the orange color) stand for the following morphologies:

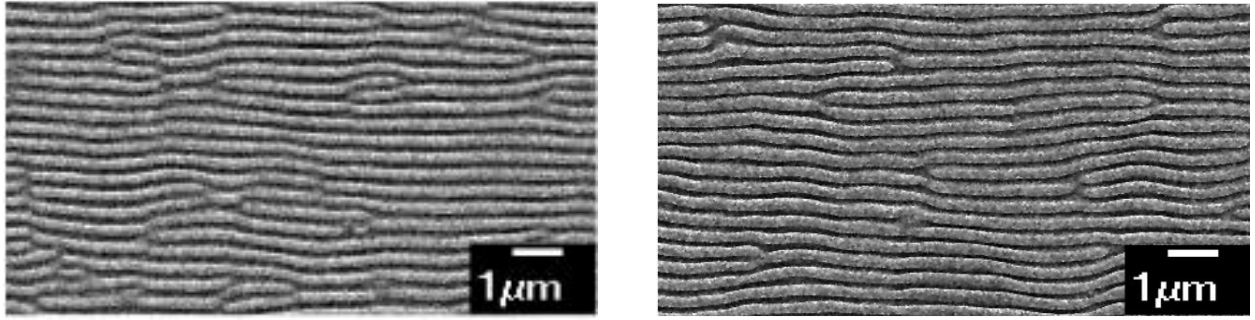


Figure 4.5: SEM pictures of -uniform LSFL. Left: Fluence= 0.4 J/cm^2 , 25pps. Right: Fluence= 0.3 J/cm^2 , 50pps.

We conclude that uniform LSFL parallel appear for low Fluences and number of pulses in the range of (30-200). The formation of these lipss is parallel to the polarization of our laser beam. Furthermore, the non-uniform LSFL that are formed for larger fluence, and relatively same number of pulses are also parallel to the direction of beam polarization and appear small roughness.

Using the 2D-FTT transform, as explained previously, we calculated the Period for each of the periodical structures that were captured. Then, we made a chart of Periodicity over Number of Pulses, with fixed

Fluence, both for the non-uniform LSFL and uniform LSFL, so that we would have a clear view of how periodicity behaves when changing the Number of Pulses in the material.

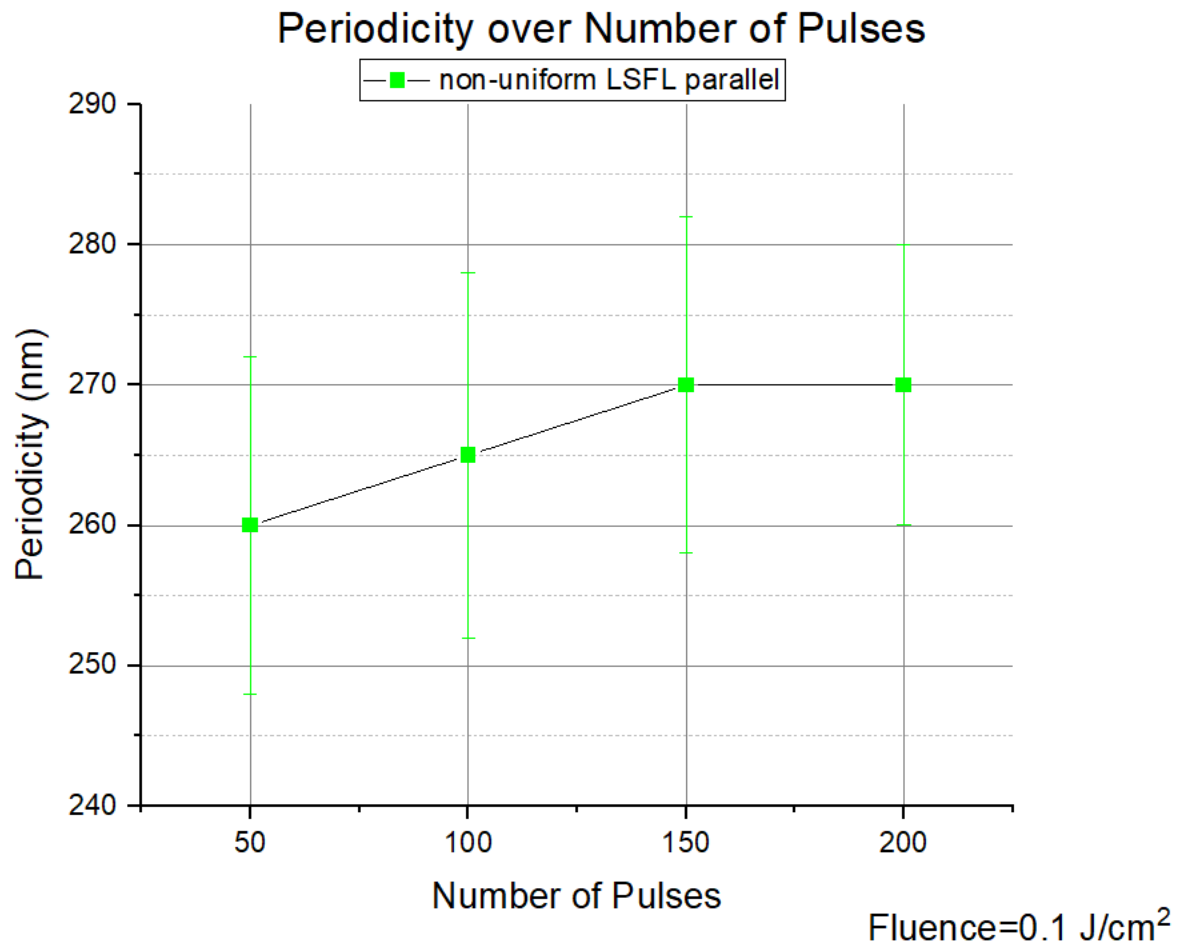


Chart 4.5: Periodicity over Number of Pulses chart, with constant Fluence=0.8 J/cm² for the non-uniform LSFL that were performed in Polycarbonate using 257nm wavelength (fs laser) and linear polarization.

As it is presented in the Chart 4.5, when increasing the number of pulses, the periodicity on the non-uniform LSFL, using 342nm, increases. We can see that the values appearing, are between the range of (260-270) nm, a little beat above the wavelength of our laser beam, something we may expected because of their non-uniform morphology.

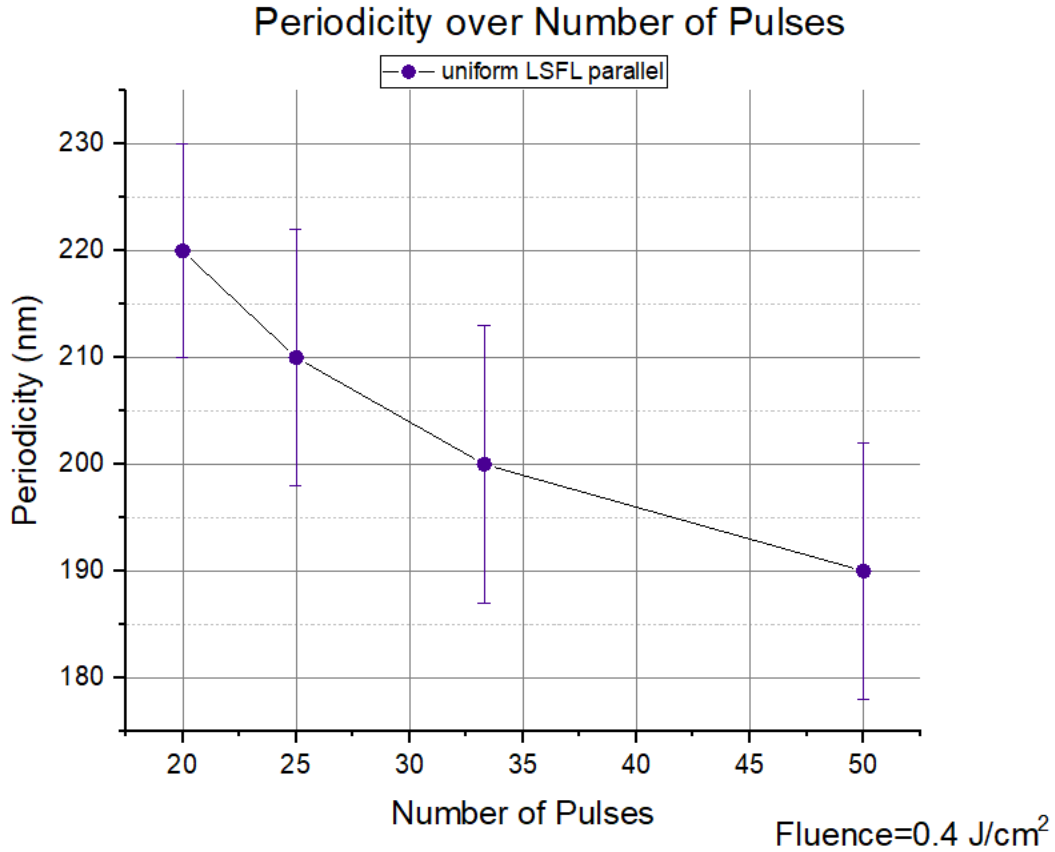


Chart 4.6: Periodicity over Number of Pulses chart, with constant Fluence=0.4J/cm² for the non-uniform LSFL that were performed in Polycarbonate using 257nm wavelength (fs laser) and linear polarization.

In the same way we studied the spikes-like structures, setting a constant Fluence of 0.1 J/cm² (Chart 4.6). In this case we can see the same behavior as before, while the number of pulses increases the periodicity of the structure's increases too. This outcome is logical as we study the same type of structures but in its uniform morphology. Moreover, the periodicity in this case declines -compared to the one in the non-uniform morphology. Now, we have a period range of (190-220) nm smaller than the period of non-uniform LSFL and the laser beam wavelength.

4.3 Dots Formation on Polycarbonate using 4th harmonic and Analysis

Finally, we proceeded in using the 4th harmonic generation of the laser, to study the structures that could be formed, changing the polarization using a $\lambda/2$ waveplate, from liner to circular. The wavelength in this case is equal to 257 nm and a morphological map of all the structures that were created is presented below.

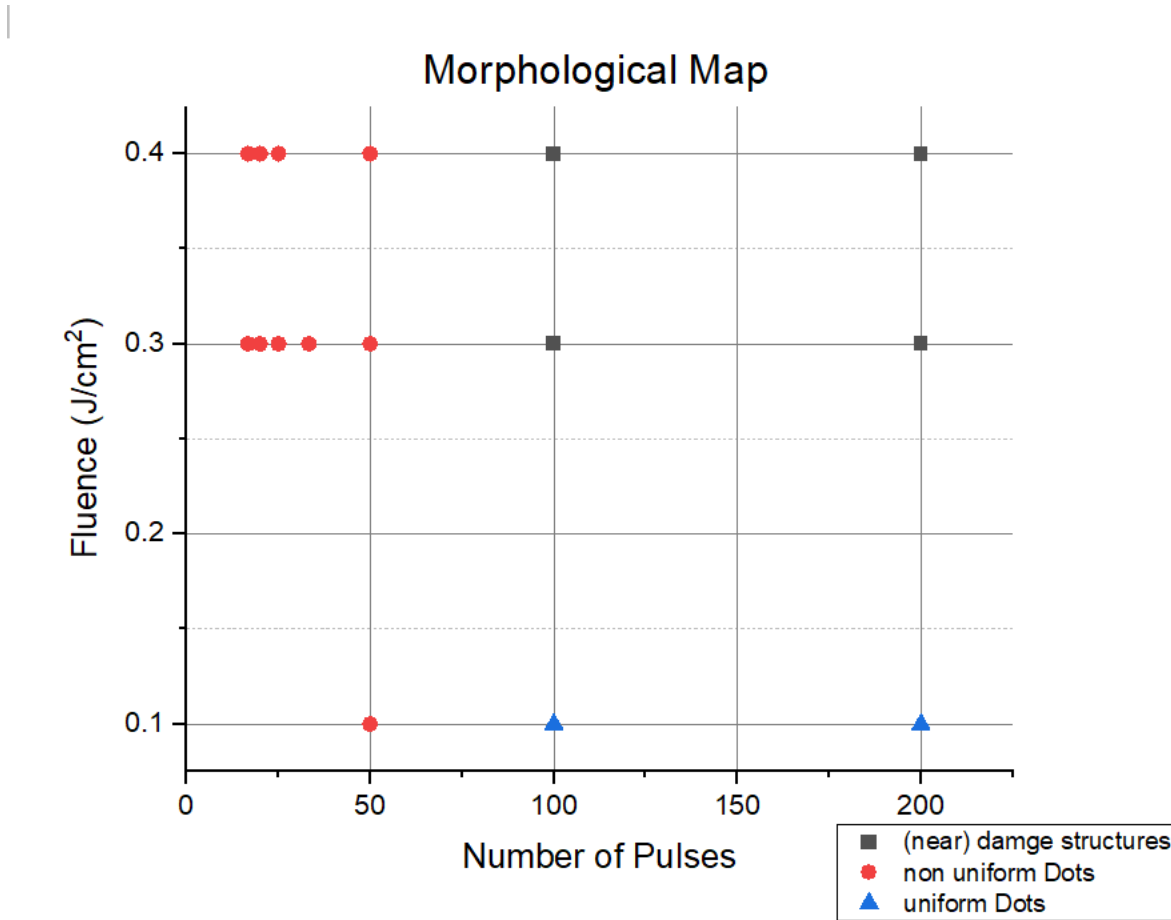


Chart 4.7: Morphological Map of structures using 257nm wavelength and circular polarization in Polycarbonate material.

The *(near) damage threshold structures* (presented with green color) stand for the following morphologies:

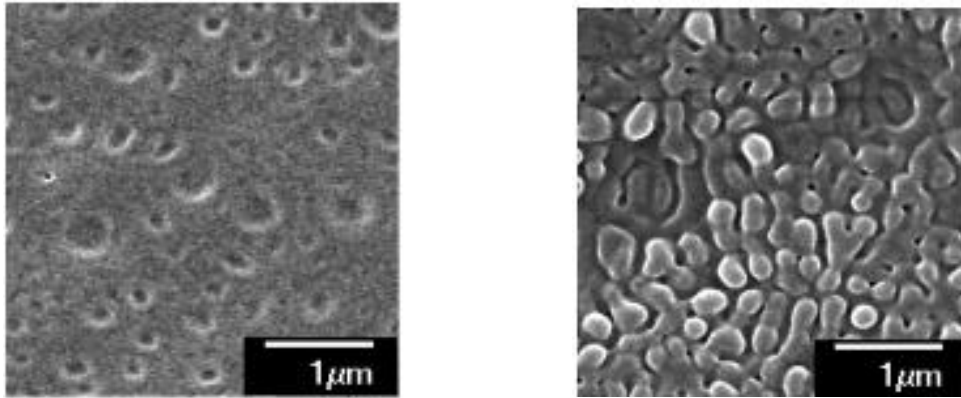


Figure 4.6: SEM pictures of *(near)damage dots*. Left: Fluence= 0.4 J/cm^2 , 33pps. Right: Fluence= 0.3 J/cm^2 , 100pps.

The *non-uniform Dots* (presented with blue color) stand for the following morphologies:

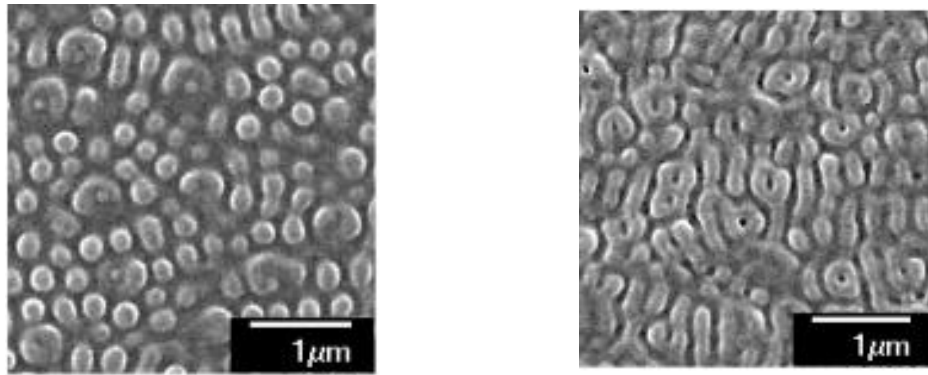


Figure 4.7: SEM pictures of *non-uniform dots*. Left: Fluence= 0.4 J/cm^2 , 25pps. Right: Fluence= 0.3 J/cm^2 , 50pps.

The *uniform Dots* (presented with orange color) stand for the following morphologies:

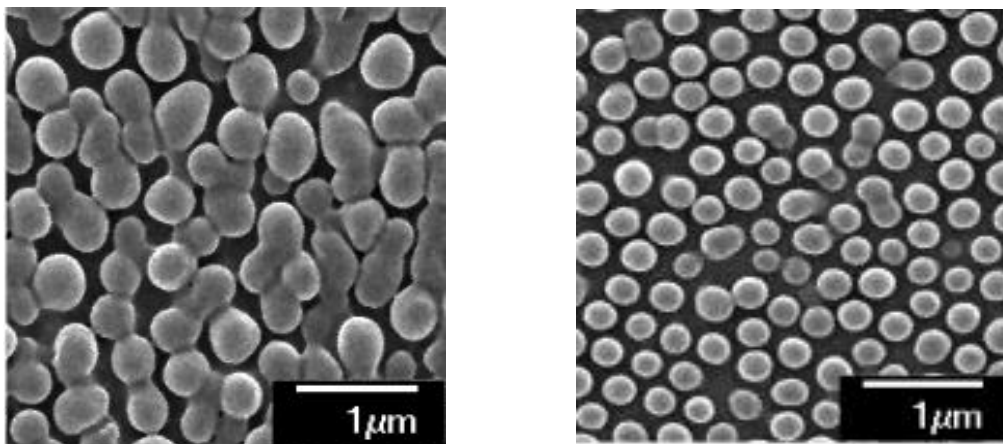


Figure 5.8: SEM pictures of *uniform dots*. Left: Fluence= 0.1 J/cm^2 , 200pps. Right: Fluence= 0.1 J/cm^2 , 100pps.

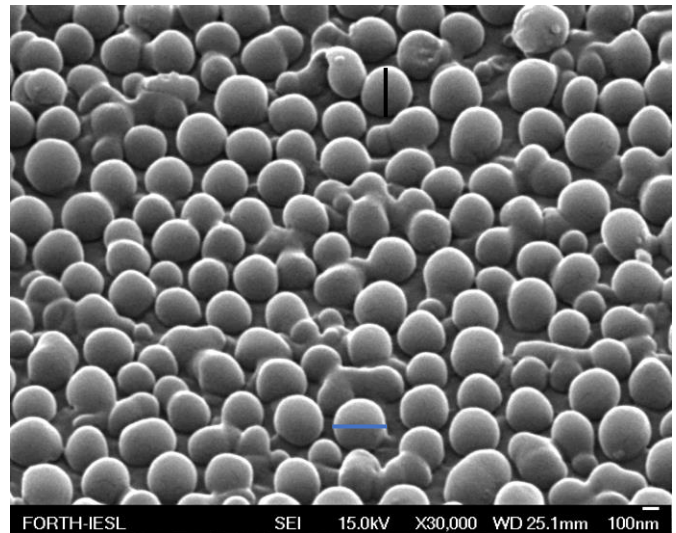
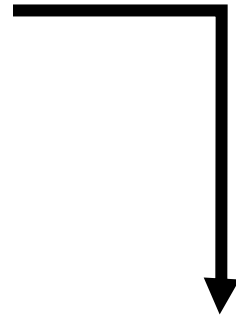
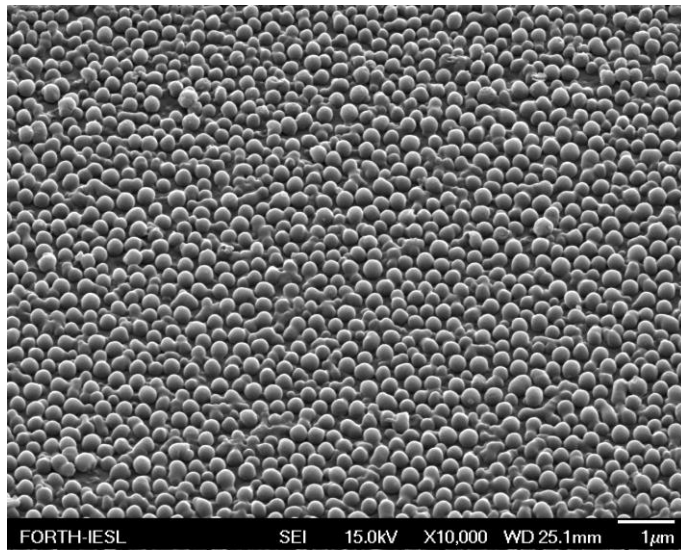


Figure 4.9: SEM tilted view of uniform dots. Fluence=0.1 J/cm², 200pps. There are two lines shaped in this picture. Black line represents the height of dots and the blue their radius.

With M. Blaxou using the tilted pictures, the following diagrams were formed to distribute the high and radius of dots.

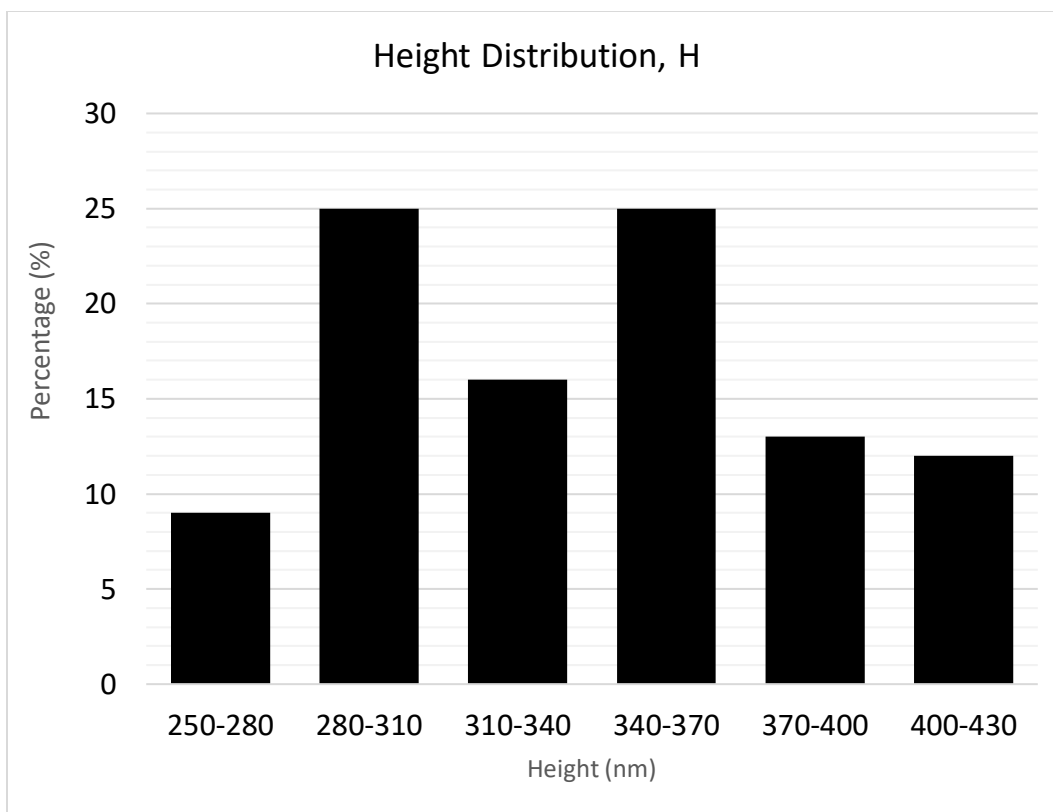


Chart 4.8: Height Distribution for Dot formation on Polycarbonate

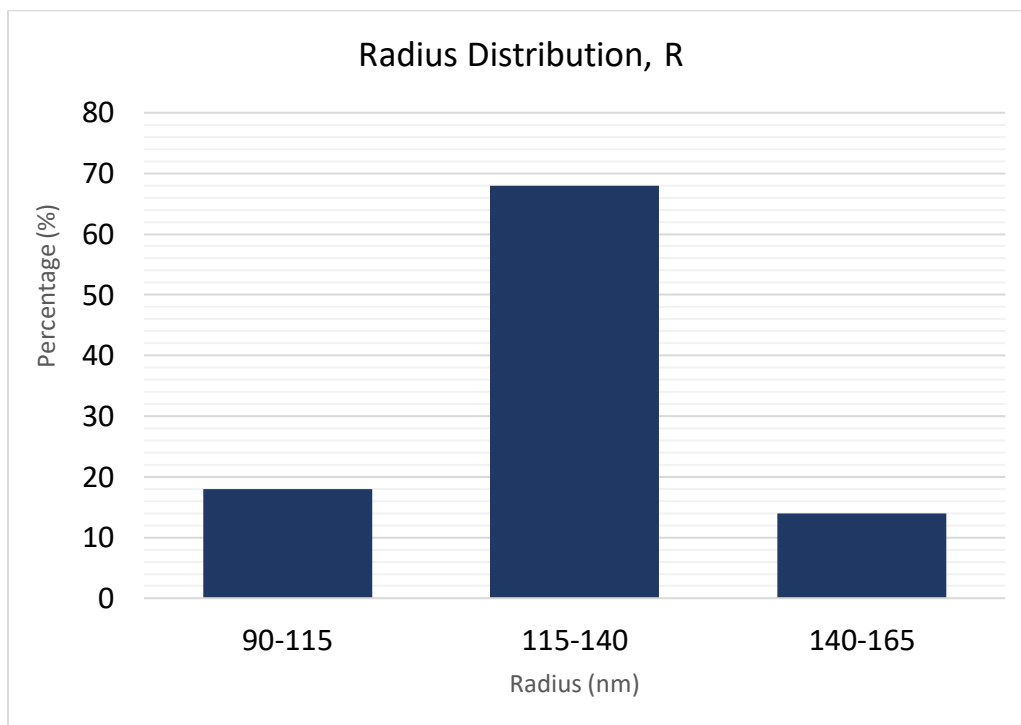


Chart 4.9: Radius Distribution for Dot formation on Polycarbonate

We can see that circular structures appear when changing the polarization from linear to circular. The region where uniform dots are performed is very limited so it's difficult to have an extended parametrical study. Uniform dots were found for low fluences $\sim 0.1 \text{ J/cm}^2$ and number of pulses in the range of 100-200. The study for dots morphology saws that most the dots' height is (280-310) nm and (340-370) nm, while their radius expands mainly to (115-140) nm.

We proceeded to the calculation of the Period for each of the non-uniform dots that were captured. Then, we made a chart of Periodicity over Number of Pulses, with fixed Fluence so that we would have a clear view of how periodicity behaves when changing the Number of Pulses in the material.

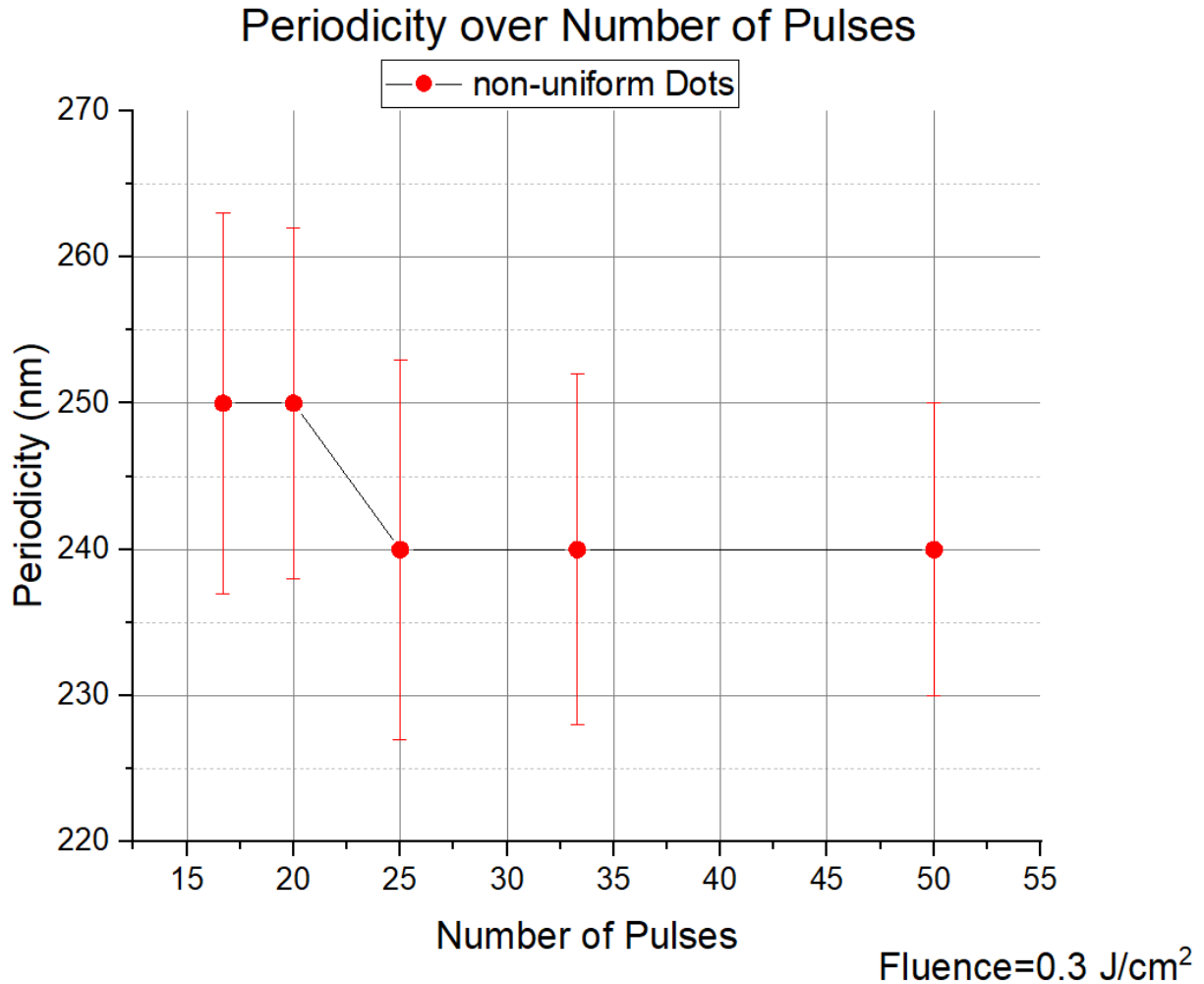


Chart 4.10: Periodicity over Number of Pulses chart, with constant Fluence = 0.3 J/cm^2 for the non-uniform dots that were performed in Polycarbonate using 257nm wavelength (fs laser) and circular polarization.

Periodicity for the non-uniform dots extends in the range of 250nm, and we could say that it stays relatively constant in the increase of number of pulses. Periodicity for the uniform dots was also calculated and was found to be 220nm.

Finally, to compare uniform LSFL to uniform Dots, we proceed to the morphological map of these two structures (Chart 4.11). In this chart we can see that there is a region of parameters (Fluence=0.1 J/cm² and number of pulses~ 200), where we can detect both morphologies.

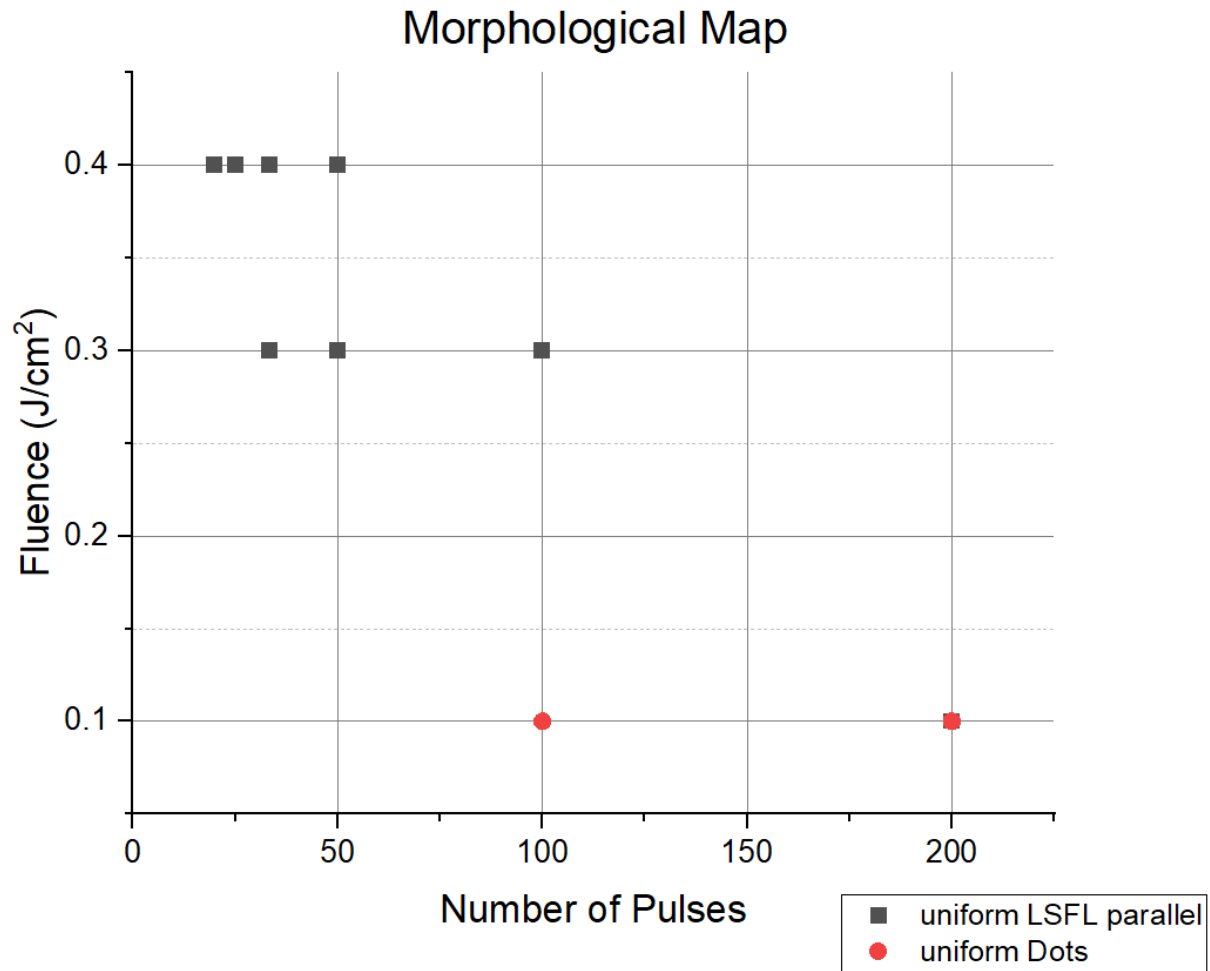


Figure 4.9 Morphological Map of structures using 257nm wavelength. Red circles stand for Dots that were performed using circular polarization and yellow square for uniform LSFL that were performed with linear polarization.

Chapter 5: Structures' Properties

5.1 Ultraviolet-Visible spectroscopy analysis on ripples and dots

Ultraviolet-Visible Spectroscopy - Theory

Spectroscopy is the study of how electromagnetic energy interacts with matter. UV spectroscopy or UV-visible spectrophotometry (UV-Vis) refers to absorption spectroscopy or reflectance spectroscopy in part of the ultraviolet and the full, adjacent visible regions of the electromagnetic spectrum.

Spectrometers are devices that are used to measure the spectra of samples. Typically, they measure the electromagnetic radiation intensity as a function of the wavelength of the radiation. The basic components of a spectrophotometer are the light source, a sample holder, a device to separate the light into its component wavelengths and a detector.

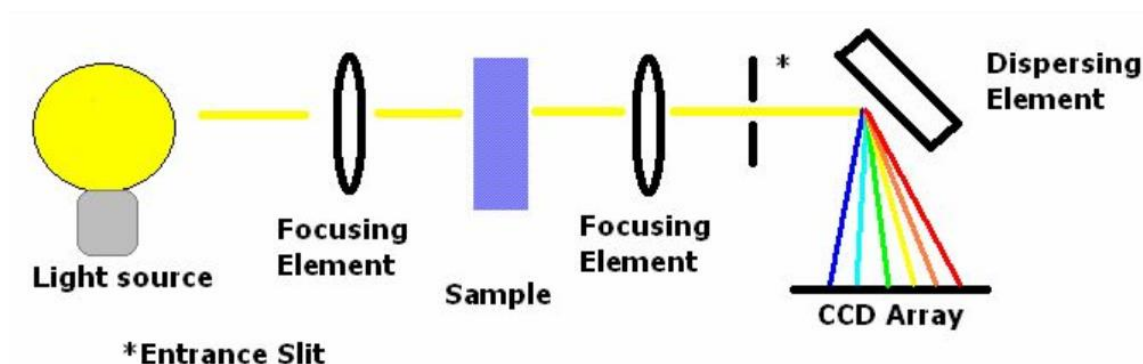


Figure 5.1: How spectrometers work

The system focuses electromagnetic energy from the light source onto the material sample. Depending upon the system configuration, light is either reflected off the sample or transmitted through it. When the light is collected from the sample, it is focused onto the entrance slit of a monochromator. The monochromator is used to separate the light by wavelength using a dispersing element, most commonly an optical grating. The light is then focused onto a charge coupled device (CCD), which is made up of individual detectors, so that the intensity of light at each wavelength may be measured. The CCD s then read-off to a computer and the result is a spectrum which displays the intensity of each wavelength of light.

UV-Vis measurements

In this study UV-Vis measurements were conducted, by M. Blaxou, on both ripple and dots structures compared to the non-irradiated surface. The results are introduced on the following charts.

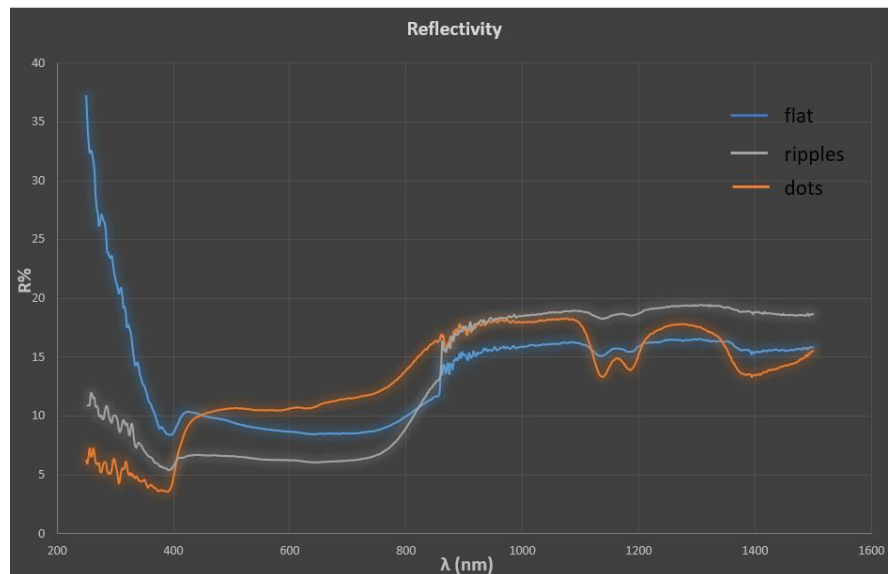


Chart 5.1: Reflectivity chart of UV-Vis for flat, ripples and dots on PC

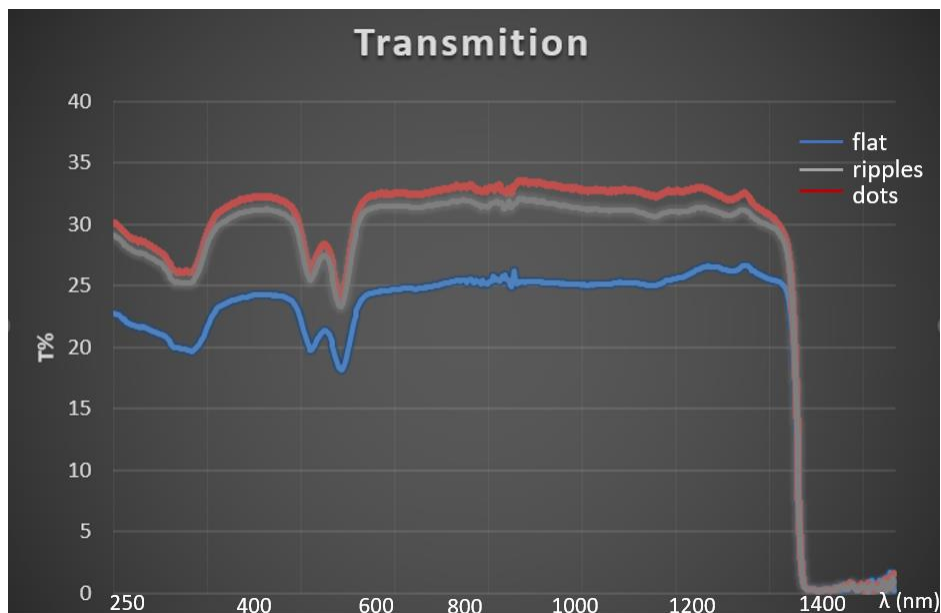


Chart 5.2: Reflectivity chart of UV-Vis for flat, ripples and dots on PC

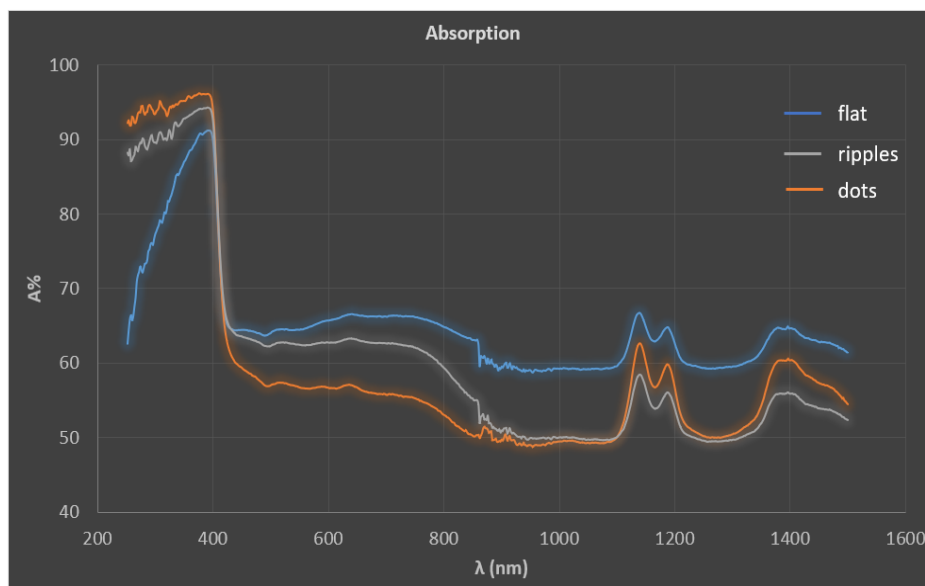


Chart 5.3: Absorption chart of UV-Vis for flat, ripples and dots on PC

Based on the above charts we can see that both structures, especially dots, adsorb better near 300-400nm wavelength, so we have a ~20% drop on the reflectivity compared to the non-irradiated area. Furthermore, based on the reflectivity chart, we can see can a curve formed from the dot-structure near 1100-1200nm wavelength.

5.2 Fourier Transform Infrared Spectroscopy measurements on ripples and dots

Fourier Transform Infrared - Theory

Fourier Transform Infrared (FTIR) is the most common form of infrared spectroscopy. All infrared spectroscopies act on the principle that when infrared (IR) radiation passes through a sample, some of the radiation is absorbed. The radiation that passes through the sample is recorded. Because different molecules with their different structures produce different spectra, the spectra can be used to identify and distinguish among molecules. In this way, the spectra are like people's fingerprints or DNA: virtually unique.

FTIS is a method that does not destroy the sample, is faster than many other techniques, sensitive and precise. It is used in organic synthesis, polymer science, petrochemical engineering, pharmaceutical industry, and food analysis. In other words, it has a wide array of applications, from monitoring processes to identifying compounds to determining components in a mixture.

The FTIR process has the following steps. A molecule's covalent bonds will selectively absorb radiation of specific wavelengths, which changes the vibrational energy in the bond. The type of vibration (stretching or bending) induced by the infrared radiation depends on the atoms in the bond. Because different bonds and functional groups absorb different frequencies, the transmittance pattern is different for different molecules (Transmittance is the flipside of absorbance). The spectrum is recorded on a graph with transmittance recorded on the Y-axis in function with the wavelength.

Fourier Transform Infrared measurements

In this study FTIR measurements were performed, by dr. I.Sakellari, on both ripple and dots structures compared to the non-irradiated surface. The results are introduced on the following charts.

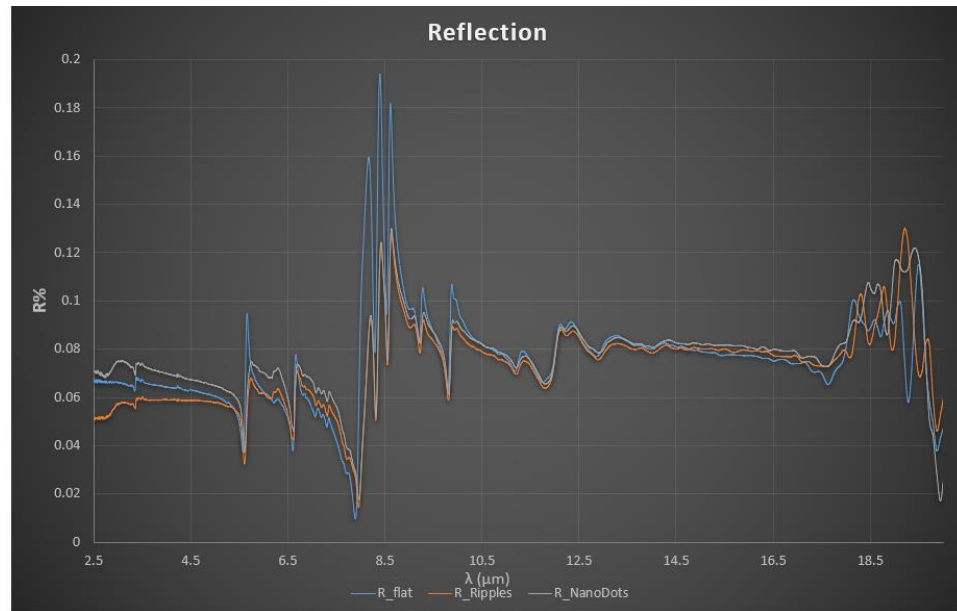


Chart 5.4: Reflectivity chart of FTIR for flat, ripples and dots on PC

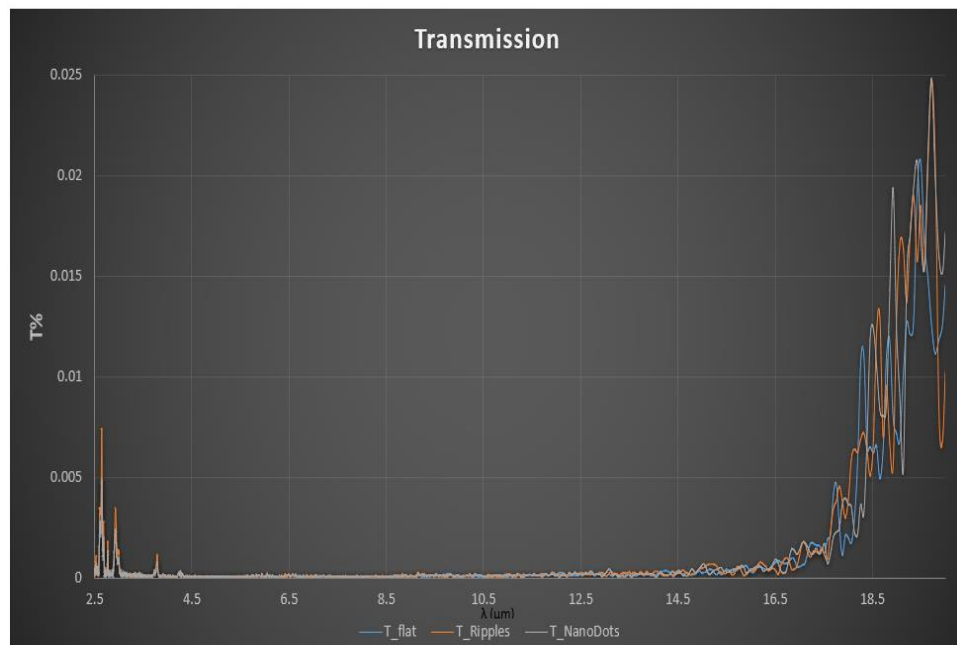


Chart 5.5: Transmission chart of FTIR for flat, ripples and dots on PC

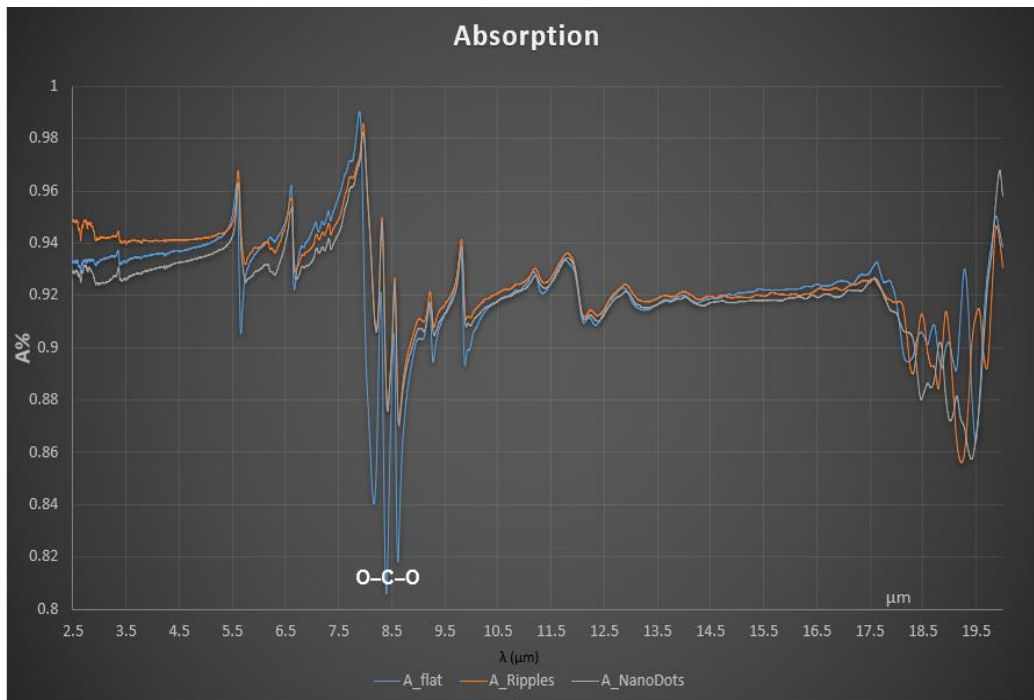


Chart 5.6: Absorption chart of FTIR for flat, ripples and dots on PC

According to the above data we can conclude that the Absorption increases of 10 % in case of both Ripples and dots.

5.3 Contact angle measurements on ripples and dots

Contact angle-Theory

The determination of solid–vapor (γ_{sv}) and solid–liquid (γ_{sl}) interfacial tensions is of importance in a wide range of problems in pure and applied science. Because of the difficulties involved in measuring directly the surface tension involving a solid phase, indirect approaches are called for: Several independent approaches have been used to estimate solid surface tensions, including direct force measurements contact angles; capillary penetration into columns of particle powder; sedimentation of particles; solidification front interaction with particles; film flotation; gradient theory; Lifshitz theory of van der Waals forces and theory of molecular interactions. Among these methods, contact angle measurements are believed to be the simplest.

Contact angle measurement is easily performed by establishing the tangent (angle) of a liquid drop with a solid surface at the base. The attractiveness of using contact angles θ to estimate the solid–vapor and solid–liquid interfacial tensions is due to the relative ease with which contact angles can be measured on suitably prepared solid surfaces. It will become apparent later that this seeming simplicity is, however, very misleading.

The possibility of estimating solid surface tensions from contact angles relies on a relation which has been recognized by Young in 1805. The contact angle of a liquid drop on a solid surface is defined by the mechanical equilibrium of the drop under the action of three interfacial tensions (Fig. 5.2): solid–vapor, γ_{sv} , solid–liquid, γ_{sl} , and liquid–vapor, γ_{lv} . This equilibrium relation is known as Young's equation:

$$\gamma_{lv} \cdot \cos\theta = \gamma_{sv} - \gamma_{sl}$$

Where θ_y is the Young contact angle, i.e., a contact angle which can be inserted into Young's equation. It will become apparent later that the experimentally accessible contact angles may or may not equal to θ_y .

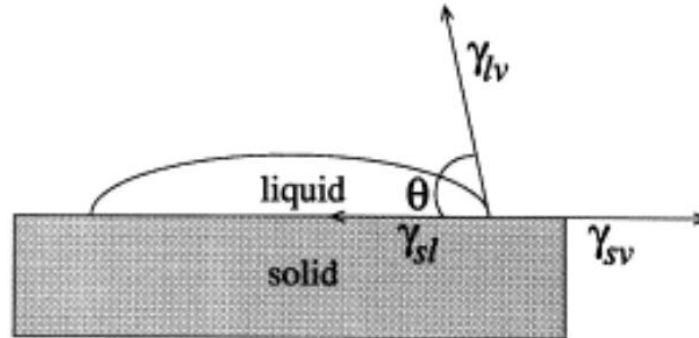


Figure 5.2: Schematic of a sessile-drop contact angle system

Regarding the above Figure When the angle the drop makes with surface is measured, the resulting angle indicates whether the drop of water is more attracted to itself or to the surface it is on. Unseen forces on the surface of the material are acting on the water drop as soon as contact is made. If these forces are strong, their pull on the water drop will cause the drop to 'wet out' or spread further over the surface. In the forces are not stronger than the attractive forces the drop has for itself, then the drop will constrict into a shape as close to a sphere as it can. These two forces are working in tandem on the drop creating an angle that can be measured. This measurement allows us to understand the relationship between the liquid drop and the surface.

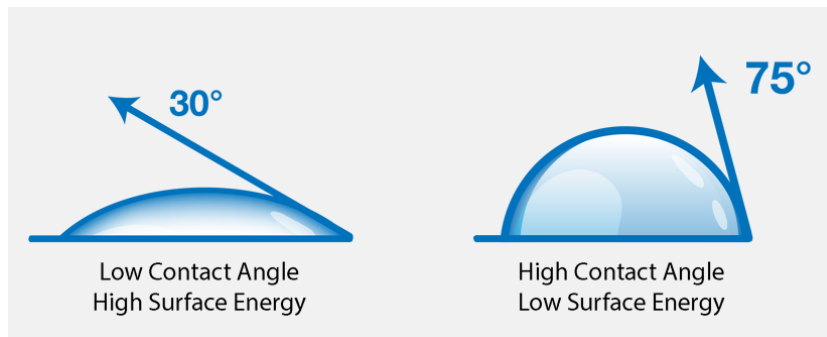


Figure 5.3

The forces acting on the drop of the water from the surface are referred to as the surface energy of the material. Of the forces are strong, the surface has high surface energy, or the surface can be said to be very energetic. This high energy pulls hard on the water, causing it to wet out. This wetting phenomenon simulates how an adhesive, paint, ink, or coating acts when placed on a high energy surface.

Contact angle as a Quality Check

Determining the contact angle will allow you to know the quality of a material surface prior to an adhesion process such as coating, sealing, soldering, adhesive bonding, printing, or painting. The contact angle can also be used as a surface quality check after cleaning processes like solvent cleaning, parts washing, ultrasonic cleaning, and more.

This angle provides quantitative data about the cleanliness of a surface at a molecular level. Sources of contamination that can create a low energy surface are oils, silicones, grease, debris, or anything that might be in a manufacturing environment that could potentially find its way onto a material surface. These contaminants are detrimental to the adhesion processes. The water drop is very sensitive to molecular differences in surface energy and, by measuring the contact angle, you can accurately predict if adhesion will occur between a coating, ink, paint, glue, primer or sealant and the surface of the material.

Contact angle can provide information to the wetting properties of a surface. In many manufacturing and assembly processes a liquid or a melted material needs to spread out adequately on a surface. In brazing and soldering, a molten metal needs to spread out over a surface of another metal; in medical diagnostics, substances like blood need to flow on a testing strip; in electronics manufacturing, a coating needs to flow into small crevices and thoroughly cover the surface of circuit boards.

Wettability is the amount to which a liquid can spread on a surface determined by the intermolecular forces between the surface and the liquid. Controlling these forces allows manufacturers to control the processes relying on the intermolecular forces.

Contact Angle measurements

Wetting properties is the quality check that we did, with S. Maragkaki, in the structures we obtained on Polycarbonate (PC). The contact angle that was formed for each structure was measured by a digital camera of the experimental set up. The drop in all cases is of 4 μ L of distilled water. The results are introduced on the following charts.

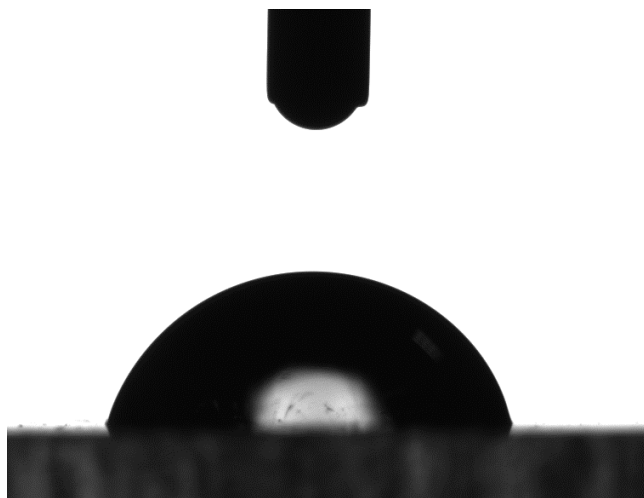


Figure 5.4: Drop that was formed on the flat area of Polycarbonate. The Contact Angle Measurement was equal to 78.48°

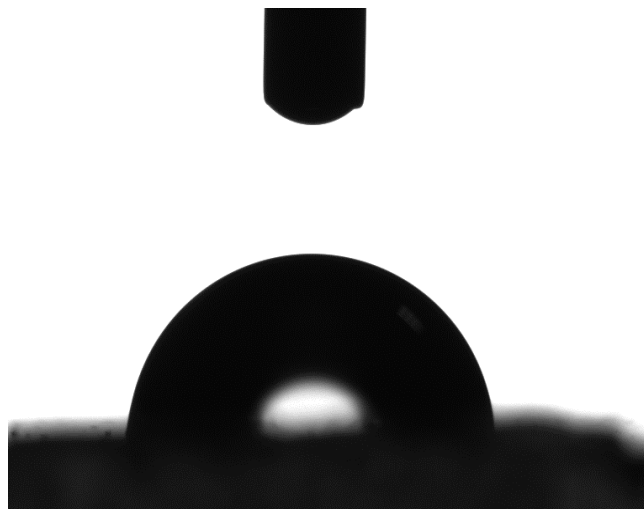


Figure 5.5: Drop that was formed on the Ripples area of Polycarbonate. The Contact Angle Measurement was equal to 83.89°

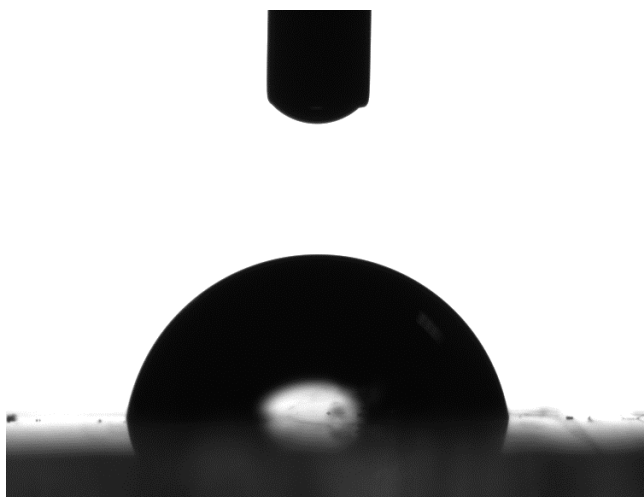


Figure 5.6: Drop that was formed on the Dots area of Polycarbonate. The Contact Angle Measurement was equal to 81.12°

As presented above the contact angle, in both cases of ripples and Dots was decreased, so the irradiated structures that were constructed saw a hydrophilic behavior compared to the flat Polycarbonate structure. Based on the above observations, and the morphology of the structures, we conclude that the surface roughness is critical for the wetting properties of the surface.

5.4 Cells' adhesion on ripples and dots

Adhesion is all around us in the natural world and is an integral feature of virtually all facets of life relating to survival, including locomotion, protection, procurement of food, and reproduction. Given the highly variable circumstances and environments under which species have evolved, it is not surprising to observe a huge variation among adhesive strategies employed by organisms. Many of these we do not understand or are not even aware of others we understand in sufficient detail to permit us to mimic in the form of synthetic adhesives.

In this study given the nature of polymers, many of whom are biodegradable, suitable for 3D scaffolds and tissue engineering, cells' adhesion was tested on both ripples and dots structures compared to the non-irradiated surface of the polymer, by dr. E. Kavatzikidou. The cells that were used were stem cells, which are undifferentiated or partially differentiated cells that can differentiate into various types of cells and proliferate indefinitely to produce more of the same stem cell.

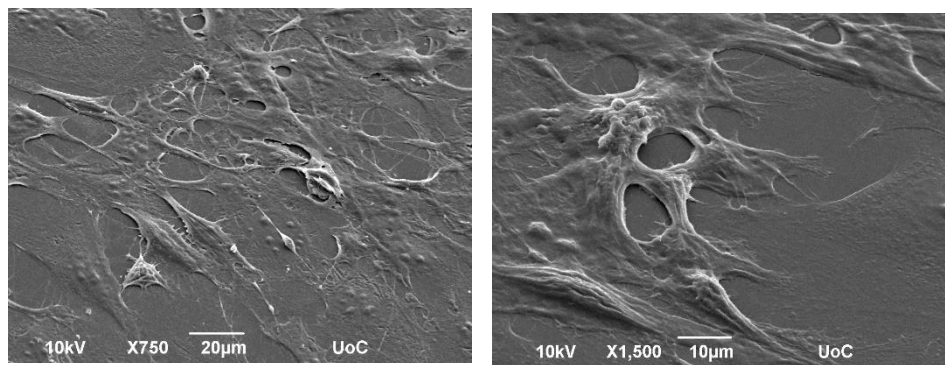


Figure 5.7: Cells' adhesion on the flat area of Polycarbonate

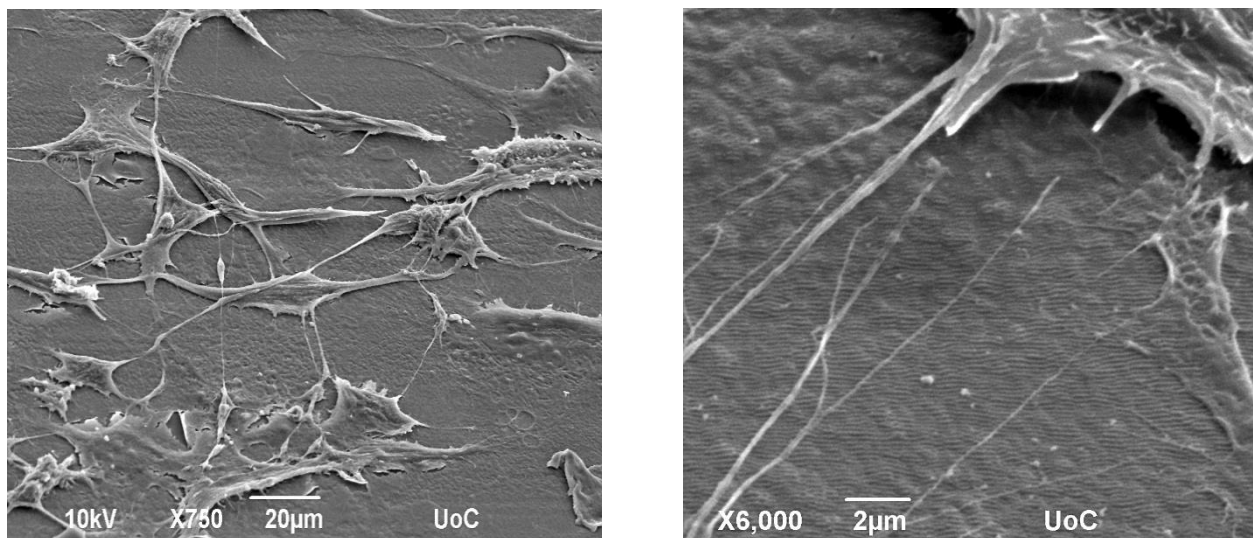


Figure 5.8: Cells' adhesion on Ripples area of Polycarbonate

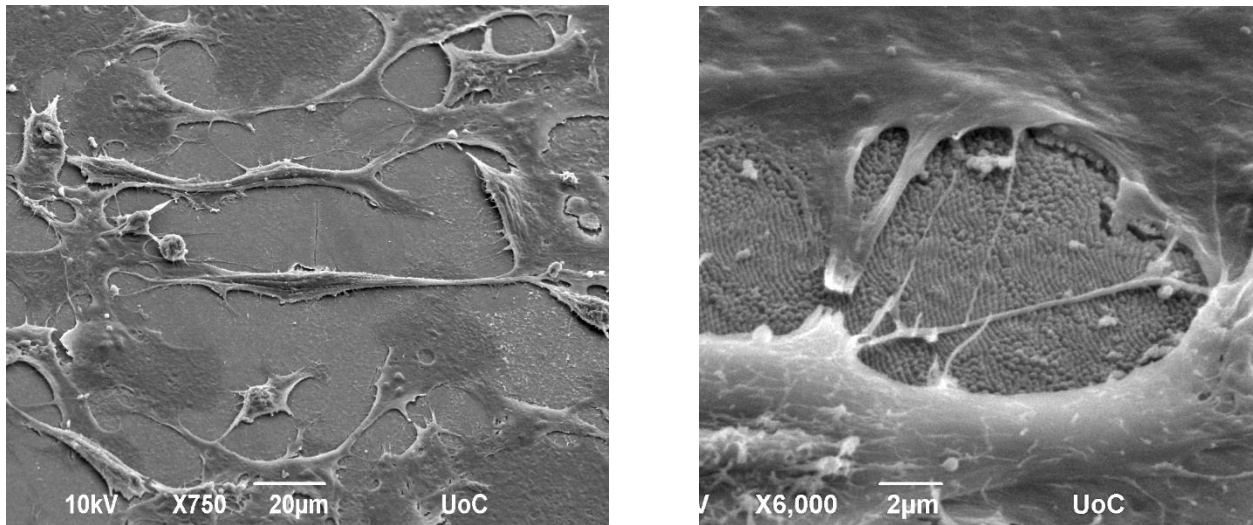


Figure 5.9: Cells' adhesion on Dots area of Polycarbonate

The cells were left to grow for 24hours and then we took AFM pictures in various magnifications.

According to the above figures we conclude that Polycarbonate itself is a friendly material for cell growth, as even in the flat, non-irradiated area, cells stay in the material. The same happens for both ripples and dots structures with not must differences in the behavior of the cells. A property that we were interested on testing was this of the directed growth of cells. Ripples are more likely to perform such a property. However, this was not possible as we can see, maybe due to the small size of our structures compared to this of the cells that were used. A type of cells with size comparative to the size of our nanostructures can be tested in future experiments to study their behavior.

Conclusion

Laser induced periodic structures on polymers opens a new, wide range of application. Nanotechnology, biotechnology, electronics, and many others, are some of the fields that this type of structures can contribute. In this thesis, main purpose was the construction of these structures and finding the quested parameters. As it was presented, there were various type of structures formed. Uniform LSFL parallel to light polarization and Dots, were the two more interested morphologies and were tested for optical, wetting and cells' adhesion properties, with interesting outcome but more studies should take place.

First of all, Dots and their parameters should be extensively studied, as the region of formation is very narrow. Furthermore, as Polycarbonate is a biodegradable material, we should consider check cells' adhesion using smaller type of cells, close to LSFL size, that could be able to influence their growth, and maybe achieve directional cells' tethering. Finally, it would be interesting to perfume these experiments on fills of polycarbonate or other polymer materials.

The further study and enhancement of LIPSS formation on polymers, will introduced more affordable and durable techniques, compared to other materials.

Bibliography

- E. Skoulas, Foundation for Research and Technology, (2020), Surface structuring of bulk and thin film materials with polarized ultrashort laser pulses
- F. Frangelakis, University of Bordeaux, (2019), Controlling and upscaling laser induced surface morphology: from tens of microns to tens of nanometers
- R.-A. Barb, C. Hrelescu, L. Dong, (2014), Laser-induced periodic surface structures on polymers for formation of gold nanowires and activation of human cells, *Applied Physics A*
- A. Rudenko, (2018), Light absorption by surface nanoholes and nanobumps, *Applied Surface Science*
- Esther Rebollar, Javier R. Vázquez de Aldana, (2013), Assessment of Femtosecond Laser Induced Periodic Surface Structures on Polymer Films, *Physical Chemistry Chemical Physics*
- Johannes Heitza, Bettina Reisinger, (2012), Laser-Induced Periodic Surface Structures (LIPSS) on Polymer Surfaces, Institute of Applied Physics, Johannes Kepler University Linz
- Qianliang Li, Walter Perrie, (2020), Femtosecond laser micro-structuring of amorphous polyether(ether)ketone at 775 nm and 387 nm, *Journal of Physics D: Applied Physics*
- Mitsuhiro Terakawa, (2018), Review: Femtosecond Laser Processing of Biodegradable Polymers, *Applied sciences – MDPI*
- Criac Technologies: Technical Support: Ultraviolet-visible-near infrared Spectrophotometry
- Brigton Science: What is Contact Angle?
- D.Y.Kwok¹A.W.Neumann, Contact angle measurement and contact angle interpretation, *Advances in Colloid and Interface Science*, [https://doi.org/10.1016/S0001-8686\(98\)00087-6](https://doi.org/10.1016/S0001-8686(98)00087-6)
- Brubaker, C. E., & Messersmith, P. B. (2012). Biological Adhesion. *Polymer Science: A Comprehensive Reference*, 211–229. doi:10.1016/b978-0-444-53349-4.00235-1
- Rebollar, E., Castillejo, M., & Ezquerro, T. A. (2015). Laser induced periodic surface structures on polymer films: From fundamentals to applications. *European Polymer Journal*, 73, 162–174. doi:10.1016/j.eurpolymj.2015.10.012
- Merck KGaA, Darmstadt, Germany and/or its affiliates: What is FTIR Spectroscopy?
- Pazokian, H., Selimis, A., Barzin, J., Jelvani, S., Mollabashi, M., Fotakis, C., & Stratakis, E. (2012). Tailoring the wetting properties of polymers from highly hydrophilic to superhydrophobic using UV laser pulses. *Journal of Micromechanics and Microengineering*, 22(3), 035001. doi:10.1088/0960-1317/22/3/035001

Acknowledgments

I would like to express my deepest gratitude to Dr. Emmanuel Stratakis for the support and for giving me the opportunity to carry out my thesis study as part of his laser processing group. I would also like to thank Dr. George Tsibidis for giving all of his support to understand and discuss the theory of laser interaction with matter, and then polymers. It is also important to thank Matina Blaxou, Stella Maragaki and Fotis Fraggelakis for their support and help in lab, and their willingness to help understand and overcome any difficulties anytime needed and Aleka Manousaki for FE-SEM time and help. Finally, I would like to thank all the members of the Ulmnp lap for their help in any way and support.